Model analysis of the $ep \to e' p\pi^+\pi^-$ electroproduction reaction on the proton

V. I. Mokeev,[1,2] V. D. Burkert,[1] T.-S. H. Lee,[3,4] L. Elouadrhiri,[1] G. V. Fedotov,[2] and B. S. Ishkhanov[2,5]

[1]*Thomas Jefferson National Accelerator Facility, Newport News, Virginia 23606, USA*

[2]*Moscow State University, Skobeltsyn Institute of Nuclear Physics, RU-119899 Moscow, Russia*

[3]*Physics Division, Argonne National Laboratory, Argonne, Illinois 60439, USA*

[4]*Excited Baryon Analysis Center, Thomas Jefferson National Accelerator Facility, Newport News, Virginia 23606, USA*

[5]*Moscow State University, Physics Department, RU-119899 Moscow, Russia*

(Received 17 August 2009; published 27 October 2009)

Recent CLAS data on the $p\pi^+\pi^-$ electroproduction off protons at $1.3 < W < 1.57$ GeV and $0.25 < Q^2 < 0.6$ GeV^2 have been analyzed using a meson-baryon phenomenological model. By fitting nine onefold differential cross-section data for each W and Q^2 bin, the charged double-pion electroproduction mechanisms are identified from their manifestations in the observables. We have extracted the cross sections from amplitudes of each of the considered isobar channels as well as from their coherent sum. We also obtained nonresonant partial wave amplitudes of all contributing isobar channels that could be useful for advancing a complete coupled-channels analysis of all meson electroproduction data.

DOI: 10.1103/PhysRevC.80.045212 PACS number(s): 13.60.Le, 13.40.Gp, 14.20.Gk

I. INTRODUCTION

Experiments with the CLAS detector at Thomas Jefferson National Accelerator Facility (JLab) have accumulated extensive and accurate data of meson electroproduction reactions on protons. Detailed experimental data have now become available for the $p\pi^0$, $n\pi^+$, and $p\pi^+\pi^-$ exclusive channels [1–11]. In addition, the first electroproduction data for the channels with smaller cross sections, such as the $p\eta$ and KY, have also been obtained with CLAS [12–16]. Review of these CLAS experimental results may be found in Refs. [17–19,21]. These data combined will allow us to determine the electromagnetic transition amplitudes for the majority of nucleon resonances (N^*) in a wide range of photon virtualities Q^2 from 0.2 to 5.0 GeV^2. The Q^2 evolution of these amplitudes contains information on the relevant degrees of freedom in the nucleon resonance structure at varying distance scales. It also allows us to explore the strong interaction mechanisms responsible for baryon formation and their relationship to QCD [22–29].

The $N\pi$ and $N\pi\pi$ exclusive channels are two major contributors to the γN and $N(e, e')$ reactions in the resonance excitation region. They are strongly coupled through hadronic interactions of the final $N\pi$ and $N\pi\pi$ states [17,20]. Thus an understanding of the reaction mechanisms for these two channels is vital for extracting the $N - N^*$ transition amplitudes at various photon virtualities. It is also a necessary first step toward the exploration of N^*'s in the mass region above 1.5 GeV using other exclusive channels with smaller cross sections, such as $p\eta$, $p\omega$, and KY. The cross sections of these weaker channels can be affected considerably by the $N\pi$ and $N\pi\pi$ channels because of the unitarity condition. The mechanisms of the $N\pi$ electroproduction have been extensively studied. The most comprehensive recent studies are by the efforts at MAMI [30,31], GWU [32], and JLab [33–36]. In contrast, the study of $N\pi\pi$ electroproduction mechanisms is still limited. In this work we try to improve the situation by analyzing the recently published CLAS data of $p\pi^+\pi^-$ channel [10].

The world data on $p\pi^+\pi^-$ electroproduction in the resonance excitation region were rather scarce before the CLAS experiments. They were limited to integrated cross sections, various invariant mass distributions, and π^- angular distributions [37]. Furthermore, the large binning in W and Q^2 does not allow the determination of N^* parameters from these data.

The first detailed measurements of $p\pi^+\pi^-$ electroproduction cross sections with CLAS were reported in Ref. [9]. The new CLAS $p\pi^+\pi^-$ data [10,11] use binnings of $\Delta W = 25$ MeV and $\Delta Q^2 = 0.05$ GeV^2 and are much more precise than those of the previous data. For the first time nine sets of onefold differential cross sections were determined in the region of $1.3 < W < 1.6$ GeV and $0.25 < Q^2 < 0.60$ GeV^2. They consist of invariant mass distributions of the final $\pi^-\pi^+$, π^+p, and π^-p and the angular distributions for all final-state particles, as will be described in Sec. II. All cross sections measured in this reaction and in others CLAS experiments may be found in Ref. [38].

Several models have been developed for analyzing the double-pion photoproduction [40–44] and electroproduction [45] reactions in the nucleon resonance excitation region, beginning with the pioneering effort of Ref. [39]. They are based on the tree diagrams of effective meson-baryon Lagrangians and have been reasonably successful in describing the very limited data of the fully integrated cross sections and the invariant mass distributions. It remains to be seen to what extent these models can describe the recent CLAS data. A comparison between these model predictions and $N\pi\pi$ cross sections (e.g., Ref. [46]) clearly showed the necessity for further improvements of reaction models to isolate the resonant contribution and to determine nucleon resonance parameters from the data. Comprehensive CLAS data on various differential $p\pi^+\pi^-$ cross open up new opportunities for phenomenological data analysis. By studying

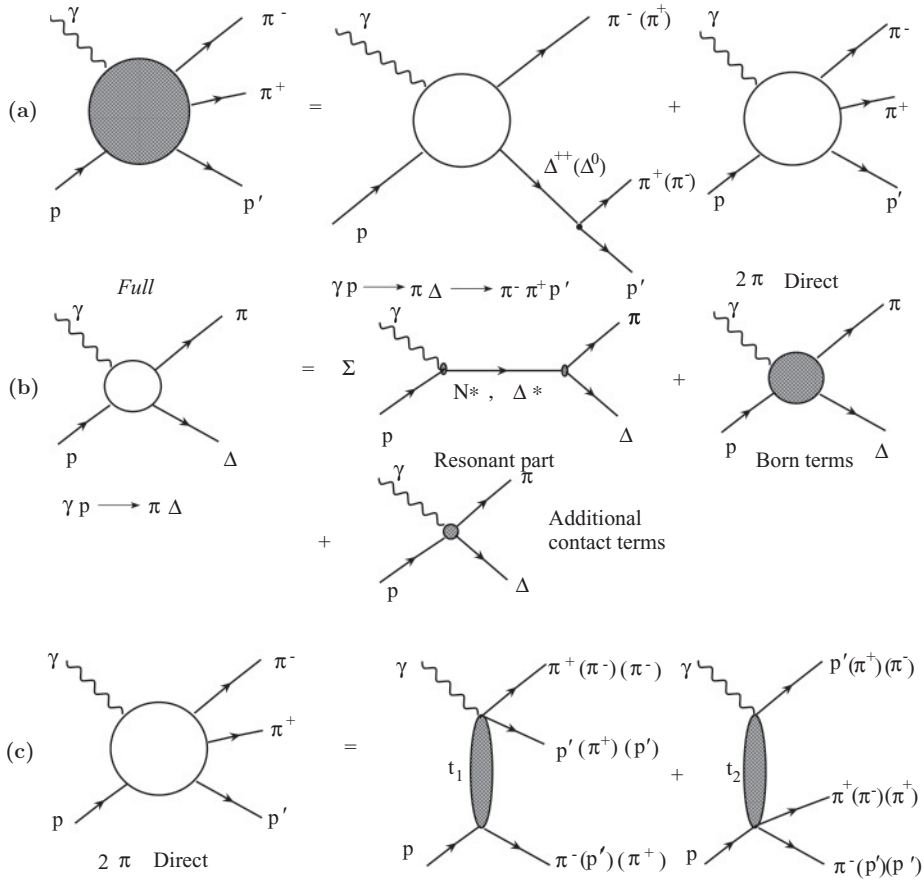

FIG. 1. The mechanisms of JM05 model [51,52] contributing to $p\pi^+\pi^-$ electroproduction in kinematic area covered by recent CLAS measurements [10] $W < 1.6$ GeV and $0.25 < Q^2 < 0.6$ GeV^2: three-body mechanisms (a), the processes contributing to $\pi\Delta$ isobar channels (b), and 2π direct production mechanisms (c).

the kinematic dependencies of the differential cross section and their correlations we are able to establish the presence and strength of the relevant reaction mechanisms and to achieve reliable separation of resonant and nonresonant contributions.

In this article we apply a phenomenological approach developed in the past several years by the Jefferson Laboratory–Moscow State University (JM) collaboration [47–56] to analyze the CLAS data [10,11] on $p\pi^+\pi^-$ electroproduction at $W < 1.6$ GeV. Within the JM model developed up to 2005, called JM05, the major part of $p\pi^+\pi^-$ production at $W < 1.6$ GeV is due to contributions from the $\pi\Delta$ isobar channels. The Δ (1232) resonance is clearly seen in all π^+p mass distributions at W > 1.4 GeV, while other mass distributions show no structures. The contributions from all other isobar channels $p\rho$, $\pi^+D^0_{13}(1520)$, $\pi^+F^0_{15}(1685)$, and $\pi^-P^{++}_{33}(1640)$ included in JM05 [50–53] are negligible in the near-threshold and subthreshold regions. Thus these channels are not included to this work. The $\gamma_v p \to p\pi^+\pi^-$ production amplitude within JM05 can then be written as

$$T_{\gamma_v N,\pi\pi N} = T^{\pi\Delta}_{\gamma_v N,\pi\pi N} + T^{\rm dir}_{\gamma_v N,\pi\pi N} \qquad (1)$$

with

$$T^{\pi\Delta}_{\gamma_v N,\pi\pi N} = \left[t^R_{\gamma_v N,\pi\Delta} + t^{\rm Born}_{\gamma_v N,\pi\Delta} + t^c_{\gamma_v N,\pi\Delta}\right] G_\Delta \Gamma_{\Delta,\pi N}, \qquad (2)$$

where G_Δ is the propagator of the Δ intermediate state and the vertex function $\Gamma_{\Delta,\pi N}$ describes the $\Delta(1232) \to \pi N$ decay. Explicit expressions for these amplitudes may be found in Appendices A–C. Contributing mechanisms in Eqs. (1) and (2) are illustrated in Fig. 1. The diagram $\gamma N \to N^*, \Delta^* \to \pi\Delta$ in the second row is the resonant term $t^R_{\gamma_v N,\pi\Delta}$ in Eq. (2). It is parameterized as a Breit-Wigner form [47] and calculated from all well-established N^*, Δ^* states with masses less than 2.0 GeV that have hadronic decays to the $N\pi\pi$ final states. The nonresonant term $t^{\rm Born}_{\gamma_v N,\pi\Delta}$ is calculated from the well-established Born terms of $\gamma_v N \to \pi\Delta$ [39,47]. Their amplitudes are presented in Appendix A. The additional contact term $t^c_{\gamma_v N,\pi\Delta}$ was introduced in Refs. [52–54] to account phenomenologically for the other possible production mechanisms through the $\pi\Delta$ intermediate states, as well as for FSI effects. Parametrization of these amplitudes may be found in Appendix B. The diagrams in the bottom of Fig. 1 represent the direct term $T^{\rm dir}_{\gamma_v N,\pi\pi N}$ in Eq. (1) that was introduced in Refs. [51,53] to describe the direct $\gamma N \to N\pi\pi$ mechanisms. It was parameterized in JM05 [51,53] in terms of a contact vertex and a particle-exchange amplitude. The parametrization of this term in JM05 will be given explicitly in Sec. III.

In this article, we have further improved the JM05 model to fit the new CLAS data on $p\pi^+\pi^-$ electroproduction cross sections. The CLAS $p\pi^+\pi^-$ data allowed us to extend considerably our knowledge of the direct production term $T^{\rm dir}_{\gamma_v N,\pi\Delta}$ of Eq. (1) in the low-W and low-Q^2 regions. The resulting model, called JM06, describes successfully all available CLAS and world $p\pi^+\pi^-$ electroproduction data

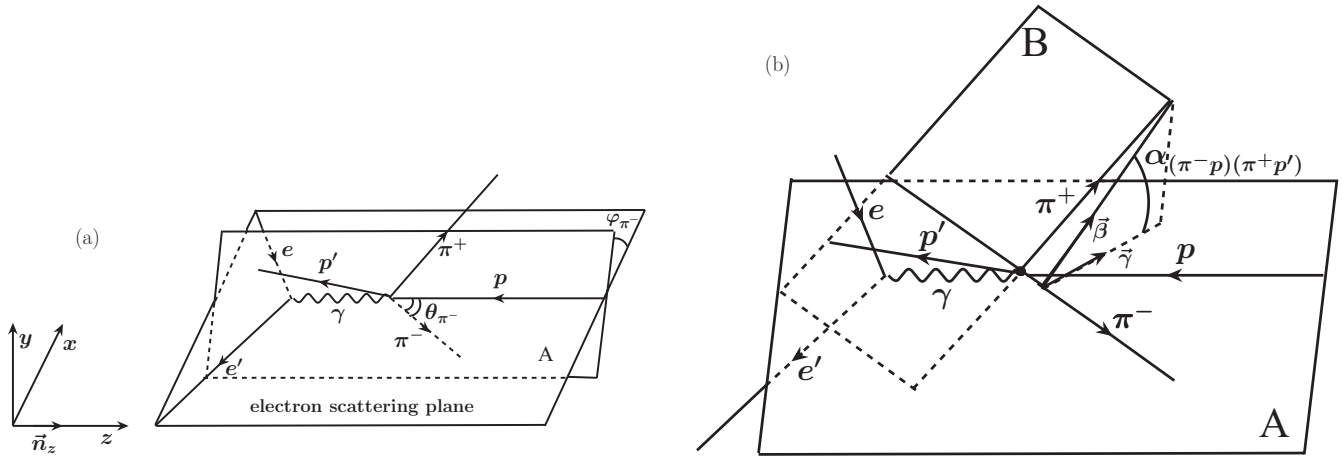

FIG. 2. The kinematics variables for description of $ep \to e'p'\pi^+\pi^-$ reaction in the center-of-mass frame of the final hadrons (first assignment presented in the Sec. II). The top plot (a) shows π^- spherical angles θ_{π^-} and φ_{π^-} while the bottom plot (b) shows angle $\alpha_{[p\pi^-][p'\pi^+]}$ between two planes: one of them (plane A) is defined by the three-momenta of the initial proton and the final π^-, and a second (plane B) is defined by the three-momenta of the two others final hadrons π^+ and p.

at $W < 1.6$ GeV and Q^2 from 0.25 to 0.6 GeV^2. A good description of the data of nine differential cross sections with rather different manifestations of contributing mechanisms in these observables enables us to establish all essential $p\pi^+\pi^-$ electroproduction mechanisms in this kinematic domain. In particular, it allows us to isolate the resonant contributions for determining the electrocouplings of the $P_{11}(1440)$ and $D_{13}(1520)$ states. Within JM06, we find that these two N^* states are the main contributors to the resonant part of the $p\pi^+\pi^-$ cross sections at $W < 1.6$ GeV.

In Sec. II, we define the kinematics of $p\pi^+\pi^-$ production. The JM06 model will be specified in Sec. III. The fitting procedures are explained in Sec. IV. Section V is devoted to discussing the results. A summary and outlook are given in Sec. VI.

II. KINEMATICS AND CROSS SECTIONS OF $p\pi^+\pi^-$ ELECTROPRODUCTION

At a given invariant mass W and photon virtuality Q^2, the cross section of the $\gamma_v p \to p\pi^+\pi^-$ reaction can be written as

$$\frac{d\sigma}{d\nu d\Omega_{e'}} = \Gamma_v \int \frac{d^5\sigma}{d^5\tau} d^5\tau, \tag{3}$$

where ν is virtual photon energy in the laboratory frame, Γ_v is the virtual photon flux defined by the momenta of incoming and outgoing electrons,[1] and $d^5\tau$ is the phase-space volume of the five independent variables in the center-of-mass system of the final $p\pi^+\pi^-$ state. There are many possible choices [62] of the five independent variables. Defining M_{π^+p}, M_{π^-p}, and $M_{\pi^+\pi^-}$ as invariant mass variables of the three possible two-particle pairs in the $p\pi^+\pi^-$ system, we adopt the following three assignments:

(i) $d^5\tau_1 = dM_{p\pi^+} dM_{\pi^+\pi^-} d\Omega_{\pi^-} d\alpha_{[p'\pi^+][p\pi^-]}$, where Ω_{π^-} (θ_{π^-}, φ_{π^-}) are the final π^- spherical angles with respect to the direction of virtual photon, and $\alpha_{[p'\pi^+]p\pi^-]}$ is the angle between the plane B defined by the momenta of the final $p'\pi^+$ pair and the plane A defined by the initial proton and the final π^- (see Fig. 2);

(ii) $d^5\tau_2 = dM_{p\pi^+} dM_{\pi^+\pi^-} d\Omega_{p'} d\alpha_{[p'p][\pi^+\pi^-]}$, where $\Omega_{p'}$ ($\theta_{p'}$, $\varphi_{p'}$) are the final proton spherical angles with respect to the direction of virtual photon, and $\alpha_{[p'p][\pi^+\pi^-]}$ is the angle between the plane B′ defined by the momenta of $\pi^+\pi^-$ pair and the plane A′ defined by the momenta of the initial and final protons;

(iii) $d^5\tau_3 = dM_{p\pi^+} dM_{p\pi^-} d\Omega_{\pi^+} d\alpha_{[p'\pi^-][p\pi^+]}$, where Ω_{π^+} (θ_{π^+}, φ_{π^+}) are the final π^+ spherical angles with respect to the direction of virtual photon, and $\alpha_{[p'\pi^-][p\pi^+]}$ is the angle between the plane B″ defined by the momenta of the final $p'\pi^-$ pair and the plane A″ defined by the initial proton and the final π^+.

The emission angles for the final-state particles in the case of first assignment are shown in Fig. 2. This choice of the kinematical variables is most suitable for describing $p\pi^+\pi^-$ electroproduction through the $\pi^-\Delta^{++}$ intermediate state, which is the dominant contributor of all isobar channels in the kinematical region covered by the considered data. For the others assignments the emission angles of the final hadrons are similar to the ones given in Fig. 2. The relations between the momenta of the final-state hadrons and the five variables of the first assignment can be found in Ref. [10].

The limited statistics of the available data does not allow the use of correlated fivefold differential cross sections in the analysis. Instead, we use the differential cross sections depending on only one final kinematic variable, obtained from integrating the fivefold differential cross sections over four

[1] Explicit expressions for invariant ν and virtual photon flux Γ_v may be found in Ref. [63].

other independent kinematic variables. These differential cross sections were obtained with reasonable statistical accuracy in Refs. [9–11,56]. They are defined as

$$\frac{d\sigma}{dM_{\pi^+\pi^-}} = \int \frac{d^5\sigma}{d^5\tau_2} dM_{\pi^+p} d\Omega_{\pi^-} d\alpha_{[p\pi^-][p'\pi^+]}$$

$$\frac{d\sigma}{dM_{\pi^+p}} = \int \frac{d^5\sigma}{d^5\tau_2} dM_{\pi^+\pi^-} d\Omega_{\pi^-} d\alpha_{[p\pi^-][p'\pi^+]}$$

$$\frac{d\sigma}{dM_{\pi^-p}} = \int \frac{d^5\sigma}{d^5\tau_3} dM_{\pi^+p} d\Omega_{\pi^+} d\alpha_{[p\pi^+][p'\pi^-]}$$

for invariant mass distributions and

$$\frac{d\sigma}{d(-\cos\theta_{\pi^-})} = \int \frac{d^5\sigma}{d^5\tau_2} dM_{p\pi^+} dM_{\pi^+\pi^-} d\varphi_{\pi^-} d\alpha_{[p\pi^-][p'\pi^+]}$$

$$\frac{d\sigma}{d(\alpha_{[p\pi^-][p'\pi^+]})} = \int \frac{d^5\sigma}{d^5\tau_2} dM_{p\pi^+} dM_{\pi^+\pi^-} d\Omega_{\pi^-} \quad (4)$$

for angular distributions. Other distributions for the angles θ_{π^+}, θ_p, and $\alpha_{[p\pi^+][p'\pi^-]}$, $\alpha_{[pp'][\pi^+\pi^-]}$ are similarly defined. Overall nine independent onefold differential cross section in each bin of W and Q^2 were included in the analysis.

III. JM06 MODEL

As a starting point, we described the recent CLAS data [10] at $1.3 < W < 1.6$ GeV and $0.25 < Q^2 < 0.60$ GeV^2 within the JM05 model [51,52], which is briefly outlined in Sec. I. The relations between JM model amplitudes and charged double-pion electroproduction cross sections are presented in Appendix D. Here we specify only the input to our calculations and indicate improvements incorporated in JM06 for the analysis presented in this article.

The nucleon resonances included in the resonant term t^R of Eq. (2) are listed in Table I. The $3/2^+(1720)$ state observed in the analysis of CLAS $p\pi^+\pi^-$ electroproduction data [9] is also included there. The N^* hadronic decay widths, branching fraction to $\pi\Delta$ and ρp final states were taken in part from analysis of hadroproduction data [65] (numbers in Table I). Hadronic parameters for other states needed in the calculations of resonant amplitude t^R (symbols "var." in Table I) were taken from analysis [52] of the CLAS data [9], which covered $1.4 < W < 2.0$ GeV and $0.5 < Q^2 < 1.5$ GeV^2. The initial values of the electromagnetic form factors, $A_{1/2}(Q^2)$, $S_{1/2}(Q^2)$, $A_{3/2}(Q^2)$ were estimated from interpolations [35,52,66] of CLAS and world data to the considered Q^2 region covered by the data [10] and further adjusted in fitting the data. With these specifications, it was found that the fits at low W and Q^2 [10,11] are sensitive only to the first two N^*'s listed in the Table I. The contributions from the higher masses N^*, Δ^* states are not varied in the fits of recent CLAS data [10] collected at $1.3 < W < 1.6$ GeV and $0.25 < Q^2 < 0.60$ GeV^2.

TABLE I. List of resonances included and their hadronic properties: total decay widths $\Gamma_{\rm tot}$, branching fractions (BF) to $\pi\Delta$ and ρp final states. The quoted values are taken from *Review of Particle Properties*. The quantities labeled as "var." correspond to the variable parameters fit to the CLAS $p\pi^+\pi^-$ data [9].

N^*, Δ^*	M (GeV)	$\Gamma_{\rm tot}$ (GeV)	$BF_{\pi\Delta}$ (%)	$BF_{\rho p}$ (%)
$P_{11}(1440)$	1.440	var.	var.	var.
$D_{13}(1520)$	1.520	var.	var.	var.
$S_{31}(1620)$	1.620	0.150	62.0	29.0
$P_{33}(1600)$	var.	var.	var.	var.
$S_{11}(1650)$	1.650	0.167	2.0	3.0
$D_{15}(1675)$	1.675	0.160	53.0	0.0
$F_{15}(1680)$	1.680	0.130	22.0	7.0
$D_{13}(1700)$	var.	var.	var.	var.
$D_{33}(1700)$	1.700	0.300	78.0	8.0
$P_{13}(1720)$	var.	var.	var.	var.
$3/2^+(1720)$ cand.	var.	var.	var.	var.

Detailed expressions of the term $t^{\rm Born}$ in Eq. (2) may be found in Ref. [47] and are summarized in Appendix A. It contains the minimal set of Reggeiezed Born terms. The initial- and final-state interactions in $t^{\rm Born}$ are taken into account in absorptive approximation [67] by using a procedure developed in Ref. [47] to evaluate the absorptive coefficients from the data on πN scattering.

An analysis of the CLAS $p\pi^+\pi^-$ data at $Q^2 > 0.5$ GeV^2 [9] revealed the need of an additional contributions to $\pi\Delta$ isobar channels. These contributions were parametrized by the contact terms t^c of Eq. (2) [52,53] that have different Lorentz structure with respect to the contact interactions in the described above Born terms. The contributions from these additional contact terms were confirmed in the analysis of the recent CLAS data [10,11] at $Q^2 < 0.5$ GeV^2. This is demonstrated in Fig. 3 where the differences between the solid and dashed curves are from the t^c term. The additional contact terms t^c are given in Appendix B.

Within JM05 it was found that the $p\pi^+\pi^-$ production through the isobar channels account for 70 to 90% of the fully integrated cross sections in the nucleon resonance region. The remaining parts were assumed to be due to direct 2π production mechanism that the final $p\pi^+\pi^-$ state is produced without forming an unstable hadron in the intermediate state. Initially these direct 2π production contributions were parametrized by the three-body phase space [48,49]. Their strengths in each interval of W and Q^2 were adjusted to fit the data. However, the CLAS data on center-of-mass π^- angular distributions shown in Figs. 4 and 5 revealed steep slopes at the backward center-of-mass π^- emission angles. Such behavior is clearly incompatible with the three-body phase-space parametrization of the direct 2π pion production mechanisms. We improve this part by considering the particle-exchange processes illustrated on the left side of Fig. 6. The direct $\gamma_v N \to \pi\pi N$ term $T^{\rm dir}$ of Eq. (1) is then parameterized as [51]:

$$T^{\rm dir} = A(W)\varepsilon_\mu(q_\gamma)\overline{U}_{p'}(P_{p'})\gamma^\mu U_p(P_p)\big[(P_1P_2)e^{b(t_1^0-t_{1\,\max}^0)} + (P_2P_3)e^{b(t_2^0-t_{2\,\max}^0)}\big] \quad (5)$$

with

$$t_1^0 = (P_p - P_3)^2$$
$$t_2^0 = (q_\gamma - P_1)^2 \quad (6)$$

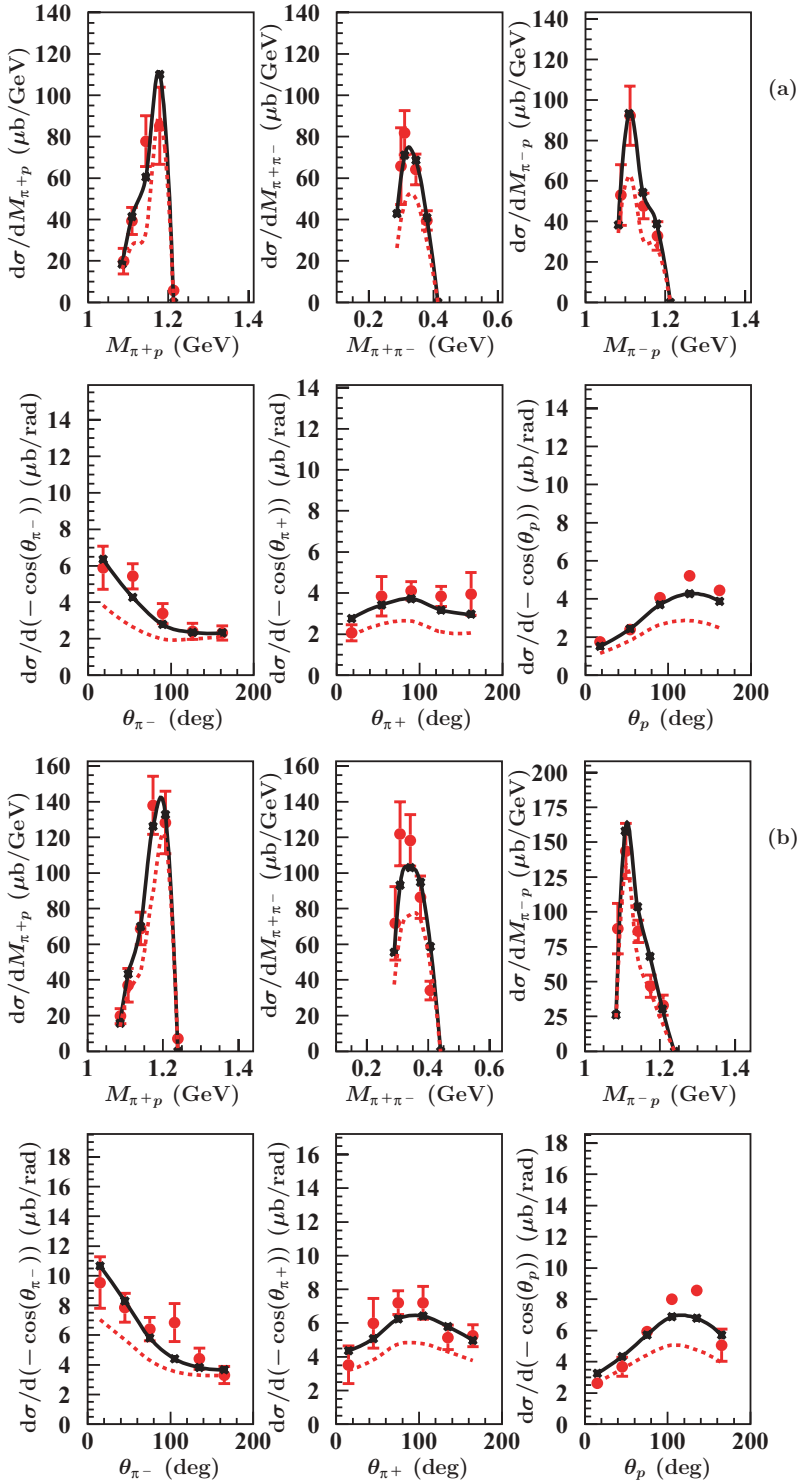

FIG. 3. (Color online) Manifestation of additional contributions to the $\pi\Delta$ isobar channels with respect to the resonant and Born terms, parametrized by extra contact terms, described in Sec. III. The data [10] at $W = 1.33$ GeV [six panels at the left side (a)], $W = 1.36$ GeV [six panels at the right side (b)] and $Q^2 = 0.425$ GeV^2 are shown by full symbols. Full JM06 calculations are shown by solid lines, while the same cross sections, calculated taking off the contributions from additional contact terms in $\pi\Delta$ channels, are shown by dotted lines.

where U_p, $\overline{U_{p'}}$ are the spinors of the initial and final protons. The first and the second terms in Eq. (5) describe the contributions from the bottom and top diagrams on the left side of Fig. 6. The P_i ($i = 1, 2, 3$) in Eqs. (5) and (6) stand for the final hadron four-momenta, shown in the bottom/top left sides of Fig. 6 by upper middle and down legs, respectively. The variables t_j^0 ($j = 1, 2$) in Eq. (6) are four-momenta-transfer square in exchange processes shown on the left sides of bottom and top rows of Fig. 6. The maximum values of t_1^0 and t_2^0 are defined as t_1^0 max, t_2^0 max, respectively. The $\epsilon_\mu \bar{U}\gamma^\mu U$ represents a Lorentz invariant coupling between the incident virtual photons and protons; the propagators of

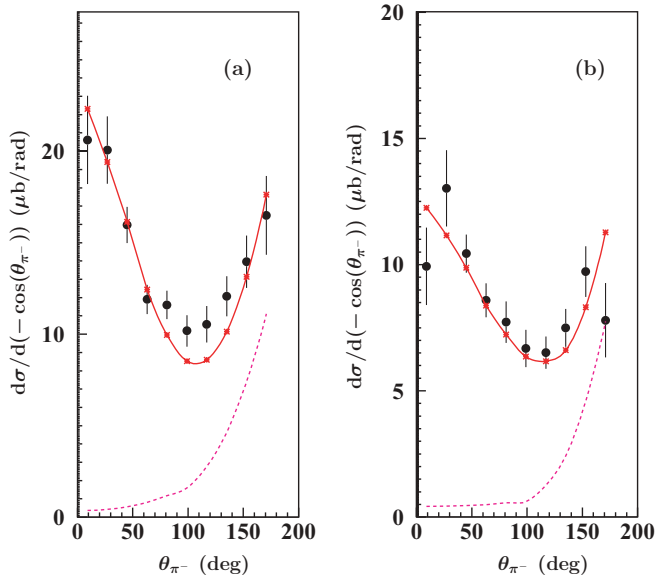

FIG. 4. (Color online) A signature of direct 2π production mechanisms, seen in the previous CLAS $p\pi^+\pi^-$ data [9]. The data on π^- angular distributions at $W = 1.49$ GeV, $Q^2 = 0.65$ GeV^2 (a) and at $W = 1.49$ GeV, $Q^2 = 0.95$ GeV^2 (b) are shown by points with error bars. The full calculation is shown by solid lines. The dashed lines correspond to the contributions from JM05 direct 2π production [51].

the unspecified exchange particles, as well as other couplings with external momenta, are parameterized as $[(P_1P_2)e^{b(t_1^0-t_1^{0\,\max})}$ (for the bottom diagram on the left side of Fig. 6) and $(P_2P_3)e^{b(t_2^0-t_2^{0\,\max})}]$ (for the top diagram on the left side of Fig. 6), the strength $A(W)$ is adjusted in the fit.

The direct 2π production mechanisms, $T^{\rm dir}$ as parameterized in Eqs. (5) and (6), are needed to describe the three invariant masses and the π^- angular distribution obtained in Ref. [9]. In particular they allowed us to describe π^- angular distributions at the backward center-of-mass angles and $Q^2 > 0.5$ GeV^2. This is shown in Fig. 4. Here we note that the steep enhancement at backward angles for the π^- differential cross sections is generated from the exponential form of the parametrization. In Fig. 5 we show that the direct 2π production term $T^{\rm dir}$ is further established in fitting the data on π^- angular distribution at $Q^2 < 0.5$ GeV^2.

The JM05 model, described above, was unable to reproduce the data on π^+ and p angular distributions. This failure has become evident at $W > 1.40$ GeV and for all photon virtualities of Refs. [10,11]. One example is shown in Fig. 7. We see that the invariant mass distributions and π^- angular distribution can be reproduced reasonably, while considerable differences remain for the π^+ and p angular distributions remain. It is therefore necessary to improve the parametrization of $T^{\rm dir}$.

In the JM06 model employed in this work, the contact interactions of the final hadron and the initial particles in two diagrams of the left side of Fig. 6 were replaced by additional exchange processes shown in four diagrams on the right side of Fig. 6. The propagators in both unspecified exchange mechanisms are parametrized by the same exponential functions of the momentum-transfer variables t_i and their slope parameter $b = 4.0$ GeV^{-2} is determined in the fit to the data. In this way we get the following parametrization for the two diagrams shown on the top right part of Fig. 6:

$$\begin{aligned} T^{\rm dir} &= A_k(W)\varepsilon_\mu(q_\gamma)\overline{U}_{p'}(P_{p'})\gamma^\mu U_p(P_p) \\ &\times (P_2P_3)e^{b(t_1-t_{1\,\max})} \\ &\times \left\{\alpha_1(W)e^{b(t_2-t_{2\,\max})} + \alpha_2(W)e^{b(t_3-t_{3\,\max})}\right\}, \end{aligned} \tag{7}$$

with

$$\begin{aligned} t_1 &= (q_\gamma - P_1)^2; \\ t_2 &= (P_p - P_3)^2; \\ t_3 &= (P_p - P_2)^2, \end{aligned} \tag{8}$$

where P_i $(i = 1, 2, 3)$ stand for four-momenta of the three hadrons, shown in the top middle diagram of Fig. 6 by upper middle and down legs, respectively, and P_p, $P_{p'}$ are four-momenta of the initial- and final-state proton. The q_γ represents the four-momentum of the initial photon, and ϵ_μ is the initial photon vector. The scalar products (P_2P_3) in Eq. (7) and (P_1P_2) in Eq. (9) were implemented to better describe invariant mass distributions for the final-state hadrons.

Two terms in the parametrization (7) correspond to the diagrams in the middle and right sides of the top row in the Fig. 6. The relative contributions from these diagrams $\alpha_1(W)$ and $\alpha_2(W)$ are determined in fits to the data under restriction $\alpha_1(W) + \alpha_2(W) = 1$. Each diagram accounts for three processes, corresponding to various assignments of the final-state hadrons shown on the right side of Fig. 6 diagrams. Full amplitude is evaluated from the coherent sum of all contributions.

Similarly, the parametrization of the amplitudes for diagrams on the right-hand side of the bottom row in Fig. 6 are from modifying Eq. (5) of the JM05 model:

$$\begin{aligned} T^{\rm dir} &= A(W)\varepsilon_\mu(q_\gamma)\overline{U}_{p'}(P_{p'})\gamma^\mu U_p(P_p)(P_1P_2) \\ &\times e^{b(t_1-t_{1\,\max})}\left\{\alpha_1(W)e^{b(t_2-t_{2\,\max})}(t_2 - t_{2\,\max})\right. \\ &\left. + \alpha_2(W)e^{b(t_3-t_{3\,\max})}(t_3 - t_{3\,\max})\right\}, \end{aligned} \tag{9}$$

where

$$\begin{aligned} t_1 &= (P_p - P_3)^2; \\ t_2 &= (q_\gamma - P_1)^2; \\ t_3 &= (q_\gamma - P_2)^2, \end{aligned} \tag{10}$$

and P_i $(i = 1, 2, 3)$ stand for four-momenta of the three final hadrons, shown in the bottom middle diagram of Fig. 6 by the upper middle and down legs, respectively. Note that the additional exponential function and the factors $(t_2 - t_{2\max})$ and $(t_3 - t_{3\max})$ in Eqs. (7) and (9) are essential to remove the discrepancies of π^+ and p angular distributions in backward and forward angles, respectively, seen in Fig. 7. After implementation of the improvements in parametrization of direct 2π production mechanisms, we succeeded in describing all differential cross section of the CLAS $p\pi^+\pi^-$ data. One example is shown in Fig. 8.

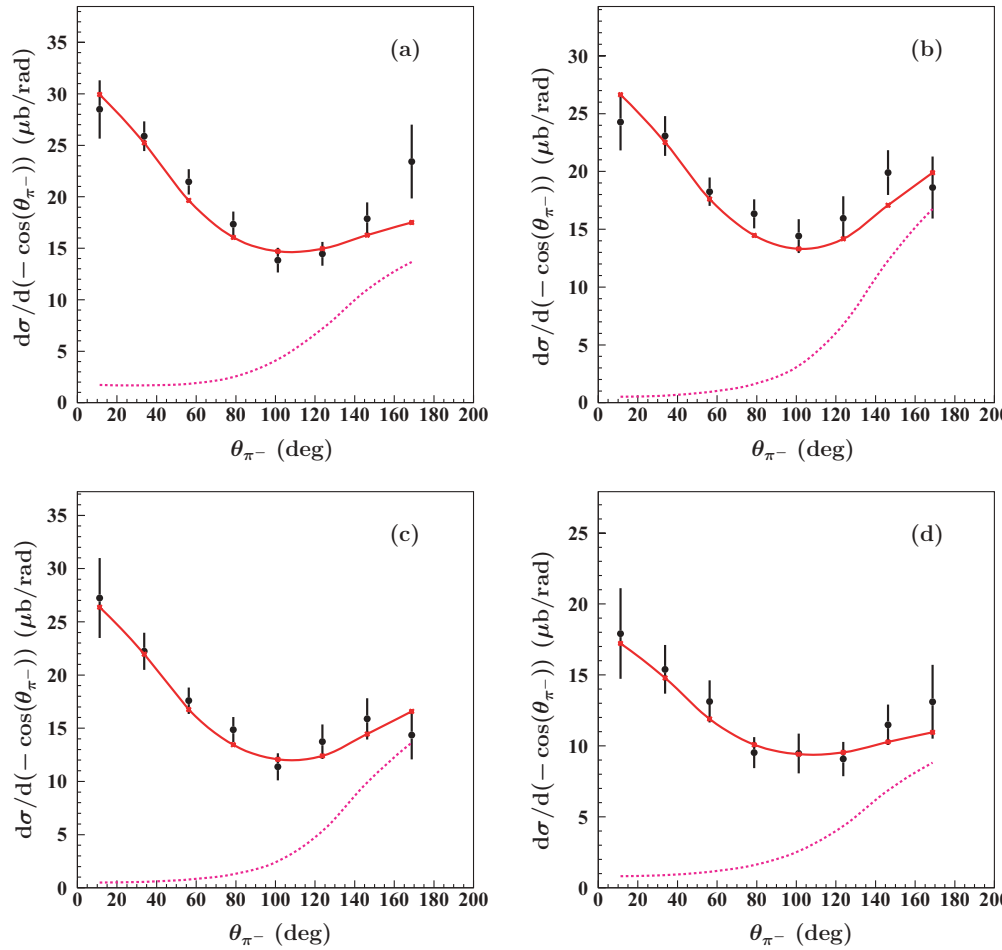

FIG. 5. (Color online) A signature of direct 2π production in the recent CLAS $p\pi^+\pi^-$ data at low W and Q^2 [10,11]. π^- center-of-mass angular distributions at $W = 1.49$ GeV, $Q^2 = 0.325$ GeV^2 (a), $W = 1.49$ GeV, $Q^2 = 0.375$ GeV^2 (b), $W = 1.49$ GeV, $Q^2 = 0.425$ GeV^2 (c), $W = 1.46$ GeV, $Q^2 = 0.525$ GeV^2 (d) and their fit within the framework of the JM05 model [52]. Full calculations are shown by solid lines, while the contributions from direct 2π processes of JM05 model are shown by dash lines.

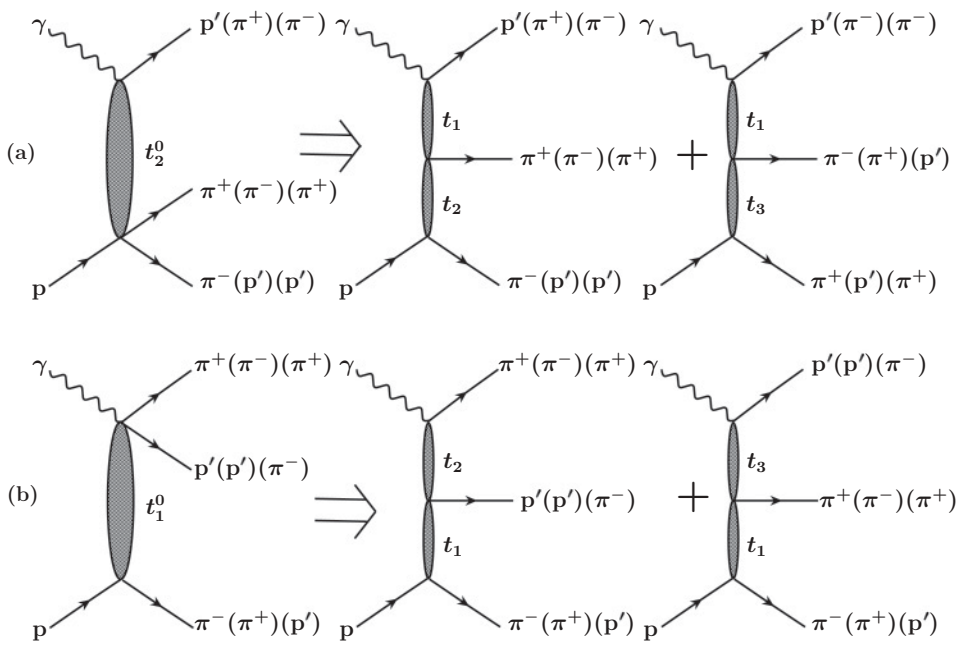

FIG. 6. Direct 2π production mechanisms of JM06 model. Top (a) [bottom (b)]: the diagrams on the left side, describing direct 2π production mechanisms of JM05 model, were replaced by diagrams, shown in the middle and right parts of the plot. Contact interaction in down (upper) vertex was replaced by additional particle-exchange amplitudes. Sets of diagrams in the middle and right parts of the plot correspond to various assignments for the four-momenta squared running over propagators in exchange amplitudes [see definitions Eqs. (7) and (9) of t_i ($i = 1, 2, 3$) for diagrams in top/bottom rows, respectively].

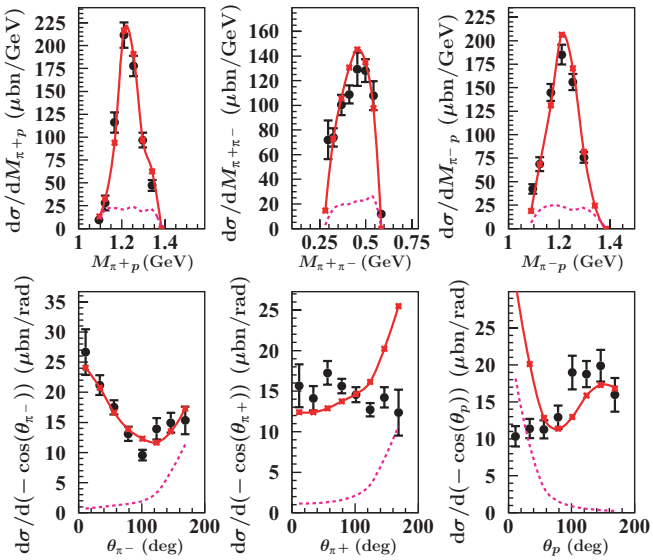

FIG. 7. (Color online) The recent CLAS $p\pi^+\pi^-$ data at $W = 1.51$ GeV, $Q^2 = 0.43$ GeV^2 and their fit within the framework of JM05 model shown by solid lines. The contributions from direct 2π production, resulting in discrepancies in the description of π^+ and p angular distributions, are shown by dashed lines.

IV. FITTING PROCEDURES

The JM06 parameters for the nonresonant mechanisms, as well as the electrocouplings and hadronic decay widths to the $\pi\Delta$ and ρp final states of nucleon resonances listed in Table I, were varied simultaneously in the χ^2 fits. In this way we accounted for correlations of resonant and nonresonant contributions in the fits.

For the nonresonant amplitudes, the $\pi\Delta$ Born terms are fixed in the fit. The magnitudes of the additional contact terms in $\pi^-\Delta^{++}$ and $\pi^+\Delta^0$ isobar channels and all direct 2π production amplitudes defined in the previous section were varied, applying different multiplicative factors to the different amplitudes. These factors were the same for all W bins inside a single Q^2 interval, while they were different in different Q^2 bins. Therefore, the W dependence of nonresonant mechanisms, established in preliminary adjustment to the CLAS data, remain unchanged in the fit, allowing us to avoid additional W-dependent fluctuations of nonresonant mechanisms that may mask the N^* contributions. The multiplicative factors were determined as random numbers normally distributed around unity with σ values in the range of 10 to 20%.

Electrocouplings of $P_{11}(1440)$ and $D_{13}(1520)$ resonances were varied within 30% of their initial values, determined in a preliminary adjustment to the CLAS data. Recent

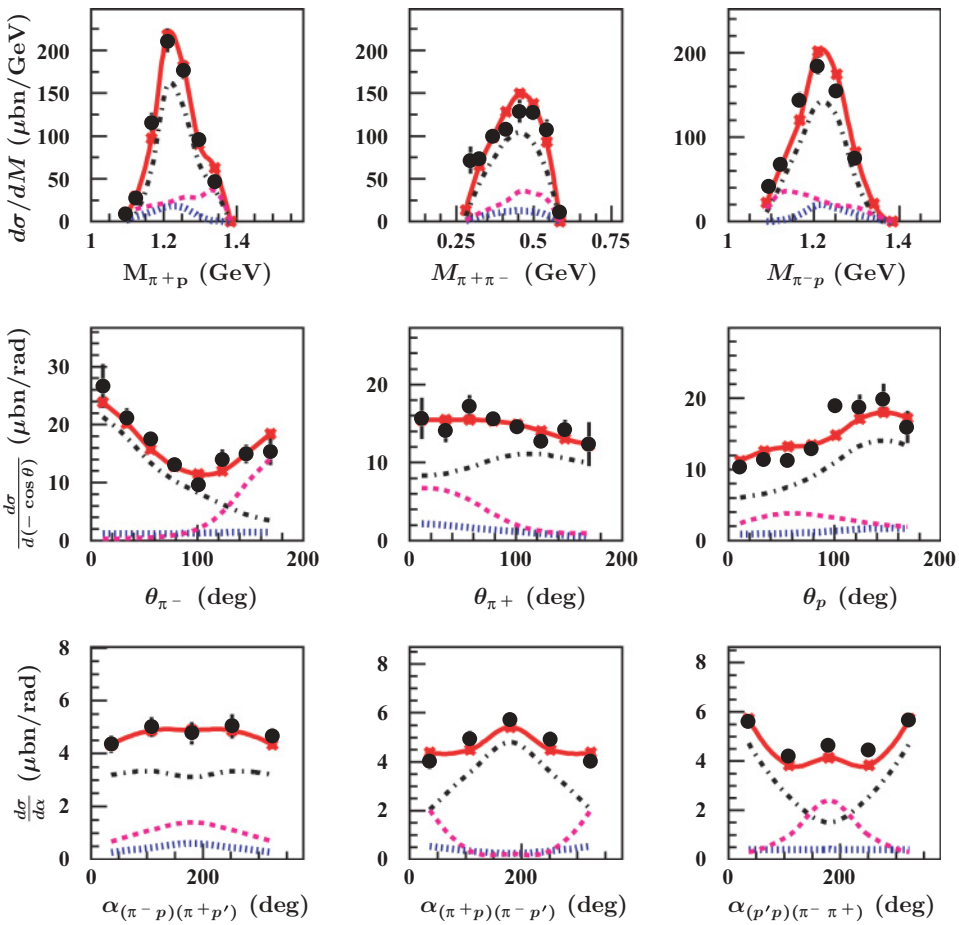

FIG. 8. (Color online) Fit of recent CLAS charged double-pion data [10] at $W = 1.51$ GeV and $Q^2 = 0.43$ GeV^2 after discussed in Sec. III improvements in parametrization of direct 2π production mechanisms. Full JM06 calculations are shown by solid lines, while the contributions from $\pi^-\Delta^{++}$, $\pi^+\Delta^0$ isobar channels, and direct 2π production are shown by dot-dash, dot, and dash lines, respectively.

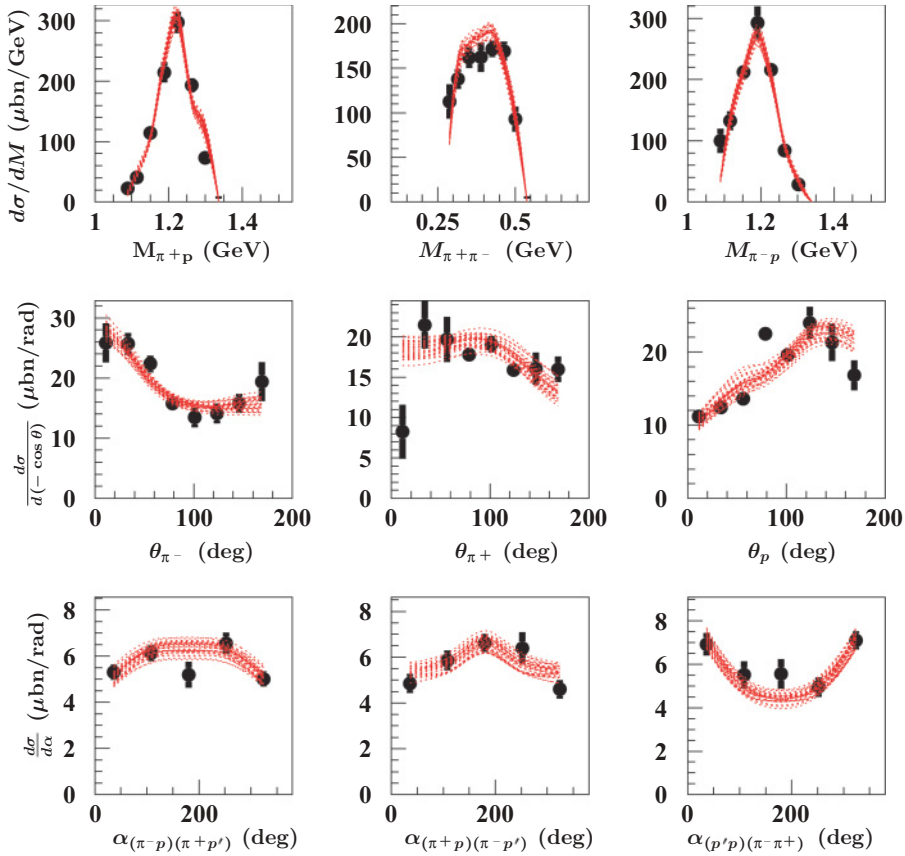

FIG. 9. (Color online) Fit of CLAS data on $p\pi^+\pi^-$ electroproduction [10] at $W = 1.46$ GeV and $Q^2 = 0.33$ GeV^2 within the framework of JM06 model. Selected in the fitting procedure calculated differential cross sections are shown by bunches of dashed lines.

analyses of the CLAS π^+n and π^0p electroproduction data [33,34] revealed zero crossing in Q^2 evolution of $P_{11}(1440)$ $A_{1/2}$ electrocoupling at photon virtualities 0.4–0.5 GeV^2. At these photon virtualities only nonzero $S_{1/2}$ electrocoupling of $P_{11}(1440)$ state affects the $p\pi^+\pi^-$ CLAS data description, while negligible $P_{11}(1440)$ $A_{1/2}$ electrocoupling values are required to reproduce the final hadron angular distributions. Electrocoupling of other states listed in Table I were fixed at the values obtained in a preliminary adjustment to the CLAS data, as described in the previous section. The $\pi\Delta$ and ρp hadronic decay widths for $P_{11}(1440)$ and $D_{13}(1520)$ were also varied in a range, which corresponds to the total hadronic decay width floating from 40 to 600 MeV. The total N^* decay widths were calculated by summing up the partial widths over all decay channels. Partial hadronic decay widths for N^*'s with masses greater than 1.55 GeV were taken from the previous analyses of charged double-pion electroproduction data [51–53]. They are independent of Q^2 and are in good agreement with the values reported in PDG [64].

With the model described above, we fit the CLAS data [10] of nine differential cross sections of $ep \to e'p'\pi^+\pi^-$ electroproduction reaction, minimizing χ^2/d.p.. A special procedure was developed to obtain not only the best data fit, corresponding to minimal χ^2/d.p., but also to establish the bands of calculated cross sections that are compatible to the data within their uncertainties. For each trial set of calculated cross sections the χ^2/d.p. value was estimated in point by point comparison between measured and calculated nine onefold differential cross sections in all bins of W and Q^2 covered by measurements. We selected in the fit all calculated onefold differential cross sections with χ^2/d.p. less than maximal χ^2/d.p.$_{\max}$, determined so that the values of selected onefold differential cross section should be inside the data uncertainties for dominant part of the data points (see example in Fig. 9). The values of resonant and nonresonant parameters of JM06 model assigned to one selected in the fit cross sections were utilized in evaluation of various isobar channel cross sections as described in the Sec V.

V. RESULTS AND DISCUSSION

Within the framework of JM06 model, we have succeeded in fitting the CLAS $p\pi^+\pi^-$ electroproduction data at low W and Q^2 [10,38].

The band of cross sections selected in fitting procedure provided reasonable data description. It may be seen from intervals of χ^2/d.p. values achieved in the CLAS data fit and listed in Table II for three Q^2 areas, where data fits were carried out. The example of data description in single bin of W and Q^2 is shown in Fig. 9. For the first time we determined in the fit the intervals of onefold differential $p\pi^+\pi^-$ cross

TABLE II. The intervals of χ^2/(data points) values corresponding closest to the data-calculated differential cross sections selected in the fit.

Q^2 interval GeV^2	χ^2/(data points)
0.25–0.4	2.71–2.80
0.4–0.5	1.77–1.87
0.5–0.6	1.39–1.65

sections that are compatible to the data, accounting for the data uncertainties.[2]

In the upper two rows of Fig. 8 we show some of the best fits (solid curves) to the three invariant mass distributions (top row), angular distributions of three outgoing particles (center row). The contributions from the $\pi^-\Delta^{++}, \pi^+\Delta^0$ isobar channels and direct two-pion production term $T^{\rm dir}$ are also shown there. The minimal χ^2/d.p. achieved in the fits of the mentioned above six onefold differential cross sections in each bin of Q^2 covered by measurements are listed in the Table III. The larger χ^2/d.p. at smallest photon virtualities are mostly related to the smaller statistical uncertainties of the data points and the fact that systematic uncertainties were not included in the fit.

To check the robustness of JM06 mechanisms, we then use the determined parameters to predict the distributions as functions of the angles α_i, defined in Sec. II, between various reaction planes. In the bottom row of Fig. 8, we see that the predicted distributions (solid curves) are in good agreement with the data. Clearly, a global fit to the differential cross-section data enables us to establish all essential $p\pi^+\pi^-$ electroproduction mechanisms at phenomenological level in the area of $1.3 < W < 1.57$ GeV and $0.25 < Q^2 < 0.6$ GeV^2 covered by the recent CLAS data [10]. No additional mechanisms are needed to describe the CLAS data in this kinematical domain.

The success of the JM06 model can also be seen in Fig. 10 comparing the calculated fully integrated cross sections with the data.

[2]To the best of our knowledge, in previous resonance analysis of electroproduction data the errors in the fit parameters were estimated assuming linear error propagation. This simplification may result in unrealistically small uncertainties in the resulting fit parameter.

TABLE III. χ^2/d.p. from the fit of all invariant mass and θ_i ($i = \pi^-, \pi^+, p$) angular distributions within the framework of the JM06 model.

Q^2, GeV^2 bin center	0.275	0.325	0.375	0.425	0.475	0.525	0.575
χ^2/d.p.	2.74	2.01	1.90	1.60	1.37	1.63	1.25

A. $\pi\Delta$ contributions

With the parameters determined from the fits (see example in Fig. 9), we now use the JM06 model to investigate the $\pi\Delta$ contributions to the $p\pi^+\pi^-$ electroproduction cross sections. This is done by examining the calculations of nine differential cross sections without including the direct two-pion production term $T^{\rm dir}$. For each selected in the data fit set of differential cross sections we evaluated the contribution from the coherent sum of the amplitudes from $\pi^-\Delta^{++}$ and $\pi^+\Delta^0$ channels. In this way we determine the bands of these partial cross sections imposed by the uncertainties of the experimental data. The coherent sum of isobar channel contributions extracted in the fit of $p\pi^+\pi^-$ cross sections in single bin of W and Q^2 is shown in Fig. 11.

We see in Fig. 11 that the $\pi\Delta$ contributions account for most of the measured cross sections. The differences are due to the direct 2π production mechanisms and their interference with $\pi\Delta$ production amplitudes. These contributions are most pronounced for the π^- production at backward angles where the direct 2π production mechanisms give the main contributions. This distinctive signature allows us to separate the cross sections generated by a coherent sum of isobar channel amplitudes and those by the direct 2π production.

In Fig. 12 we compare the contributions from each of the two $\pi\Delta$ channels. Clearly, the $\pi^-\Delta^{++}$ channel is a major contributor to the cross sections, as expected from isospin symmetry. The $\pi^-\Delta^{++}$ and $\pi^+\Delta^0$ channels exhibit rather different shapes in all nine differential cross sections, allowing us to separate their respective contributions.

Differential cross sections of individual isobar channels extracted from the CLAS data [10] may be obtained on request from the corresponding author.[3] This information will be useful for developing a more microscopic understanding of the isobar production mechanisms, such as those described in terms of explicit meson baryon diagrams [40,44,45,57–59].

B. Nonresonant partial-wave amplitudes in $\pi\Delta$ channels

Estimates for the amplitudes of mechanisms contributing to the charged double-pion electroproduction are of particular importance for N^* studies in a global multichannel analysis within the framework of advanced coupled-channels formalism, such as that developed in [57–61]. A first step foreseen in these efforts will be the combined analysis of major single and double-pion electroproduction channels. Analysis of the $p\pi^+\pi^-$ electroproduction data allowed us to obtain information on nonresonant amplitudes contributing to $\pi\Delta$ isobar channels, decomposed into a set of partial waves, described in Appendix E. They were estimated within the framework of JM06 model with parameters corresponding

[3]Dr. V. I. Mokeev, e-mail: mokeev@jlab.org.

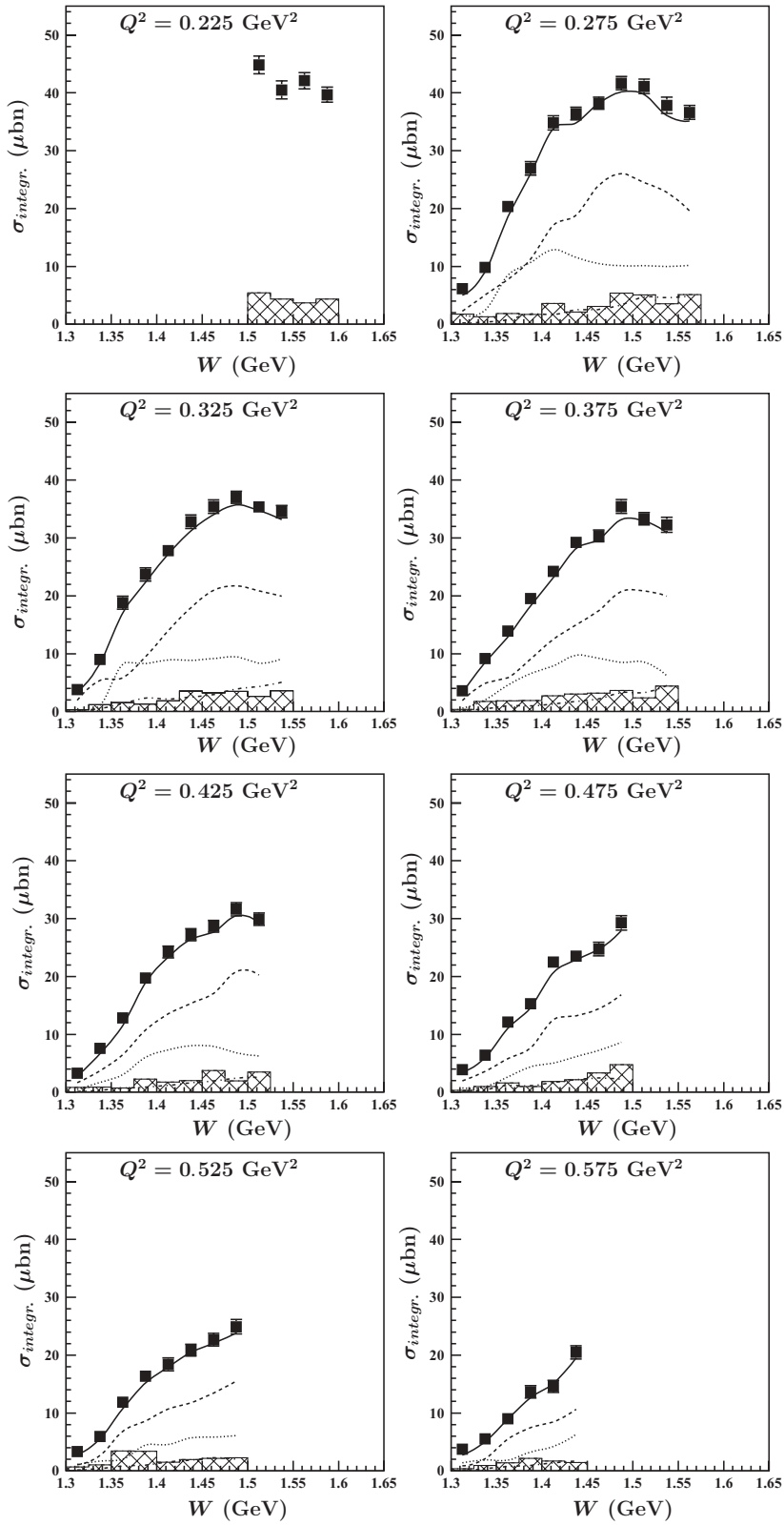

FIG. 10. The contributions from various isobar channels to the fully integrated $p\pi^+\pi^-$ electroproduction cross sections. The recent CLAS data are shown by full symbols. Shadowed areas represent the systematical uncertainties. Full calculations within the framework of JM06 are shown by solid lines. The contributions from $\pi^-\Delta^{++}$, $\pi^+\Delta^0$ channels are shown by dashed and dot-dashed lines, respectively. The contributions from direct 2π production are shown by dotted lines.

to the minimal χ^2/d.p.. Nonresonant parts of $\pi\Delta$ channel amplitudes consist of Born terms and additional contact terms described in Sec. III. The absorbtive coefficients applied to the Born term to account for ISI and FSI [47] were taken off. In this way we get the amplitudes that are nondistorted by the interactions with open inelastic channels. The partial waves for nonresonant amplitudes in $\pi\Delta$ isobar channels, derived in the CLAS data fit, are available on request to the corresponding

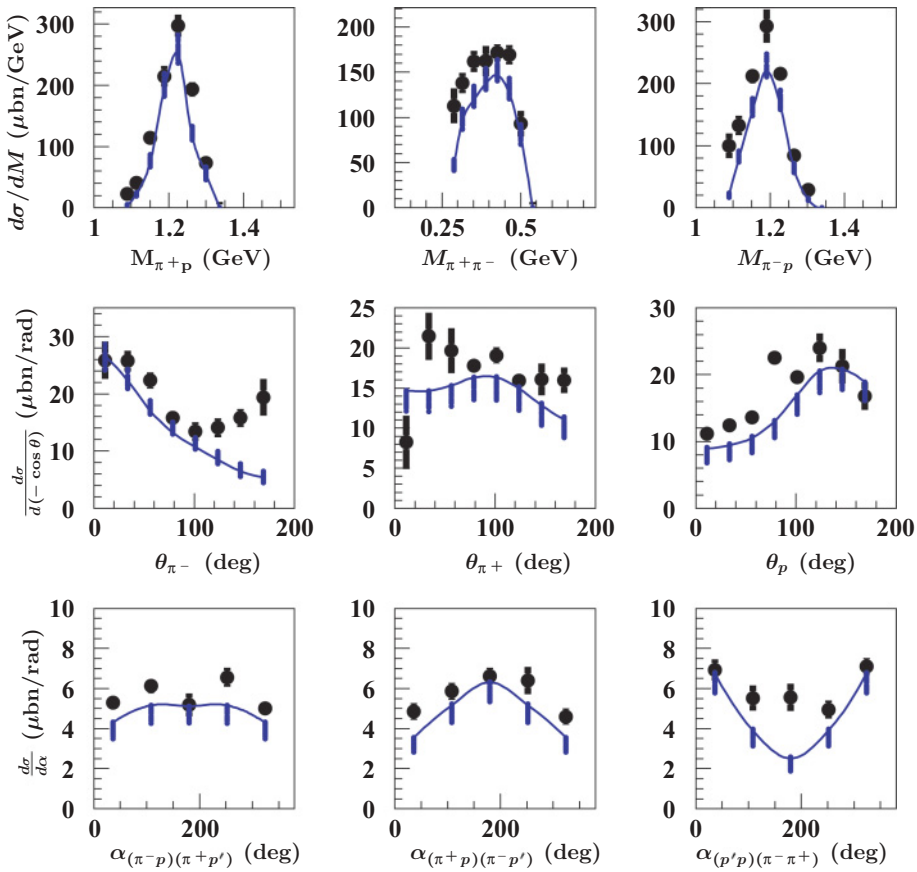

FIG. 11. (Color online) Differential cross sections for the coherent sum of $\pi\Delta$ channel amplitudes at $W = 1.46$ GeV and $Q^2 = 0.325$ GeV^2 are shown by bars connected by curves. The bar sizes represent uncertainties for these cross sections. The cross section values corresponding to the best data fit are shown by solid lines. Full symbols are the measured cross sections.

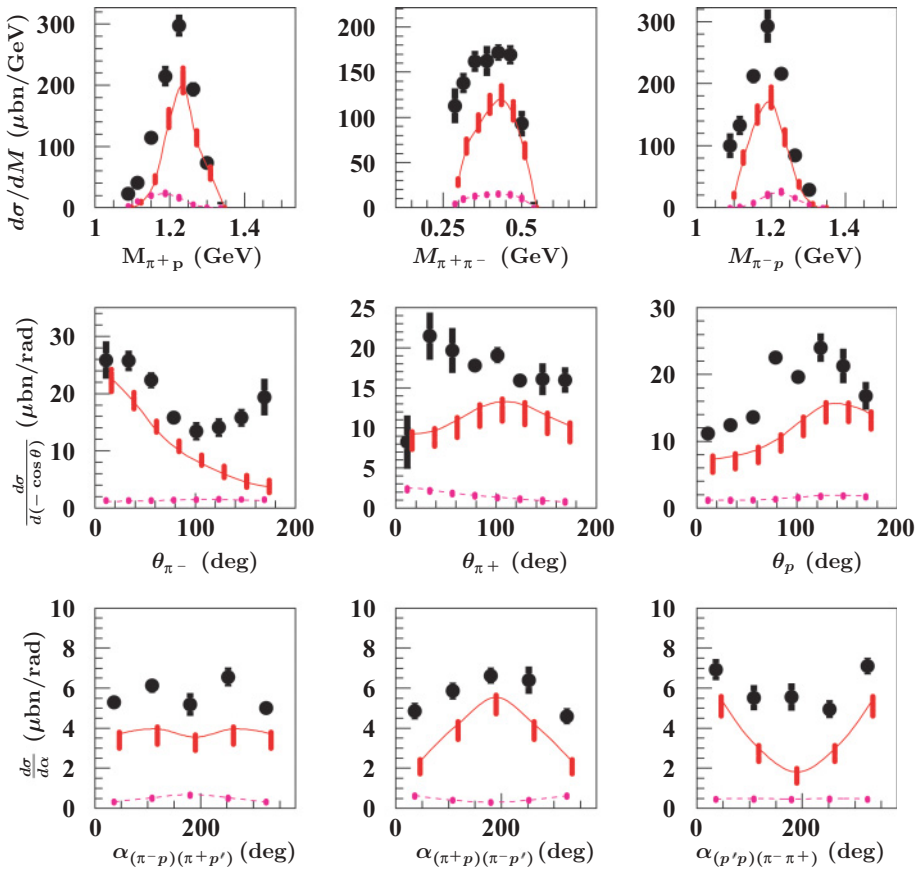

FIG. 12. (Color online) Contributions from various isobar channels to charged double-pion electroproduction obtained from the CLAS data fit at $W = 1.46$ GeV and $Q^2 = 0.325$ GeV^2. The cross sections for $\pi^-\Delta^{++}$, $\pi^+\Delta^0$ isobar channels are shown by bars connected by solid and dash lines, respectively. Full symbols are the measured cross sections. The uncertainties of bars represent the spread of the cross sections calculated with JM06 parameters determined from the fit of measured differential cross sections, as described in Sec. IV. The values connected by solid lines represent the $\pi^-\Delta^{++}$ and $\pi^+\Delta^0$ channel cross sections, estimated with JM06 parameters, that correspond to the best data fit of minimal χ^2/d.p..

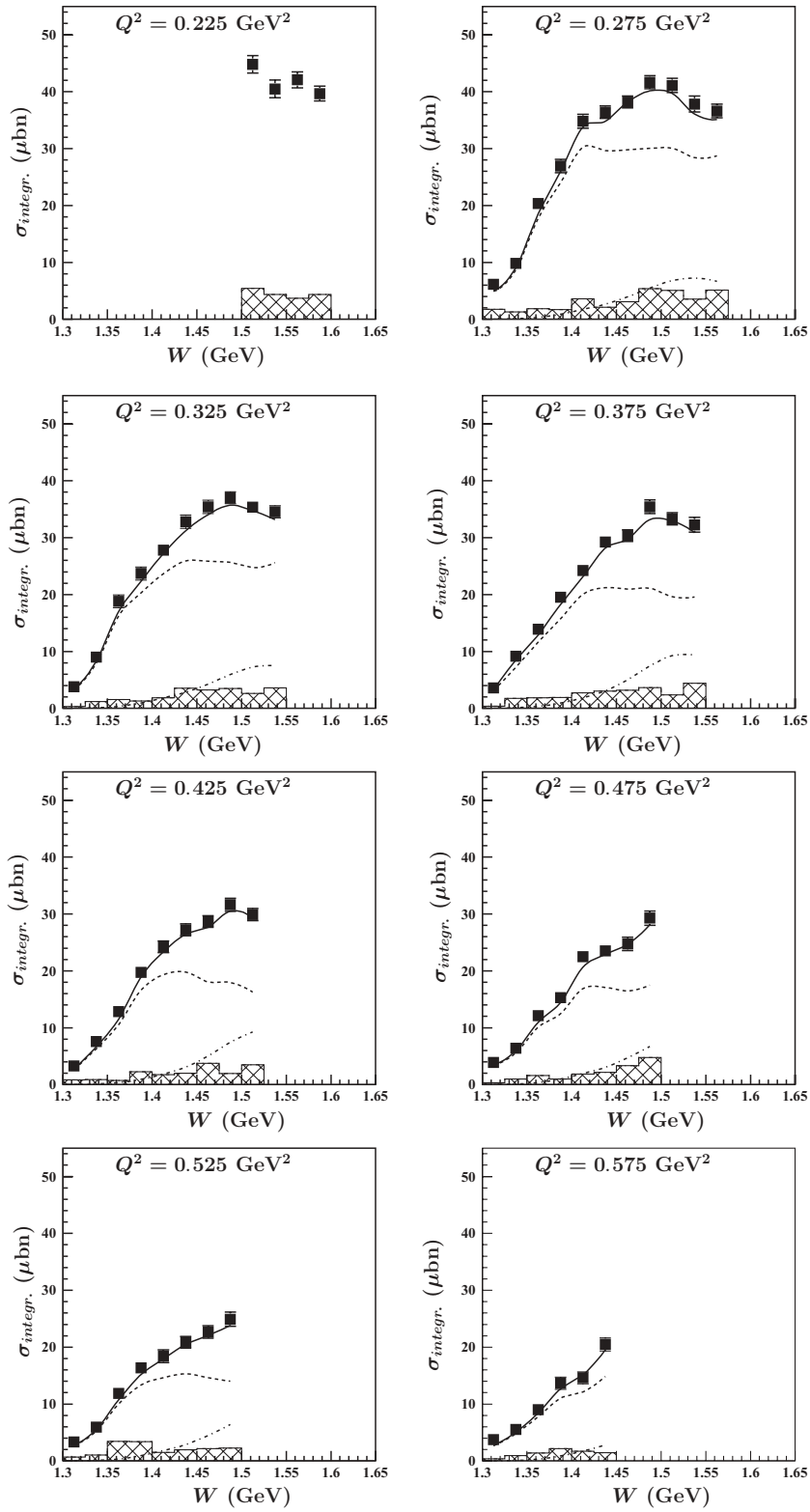

FIG. 13. Resonant and nonresonant contributions, determined from the recent CLAS data fit within the framework of the JM06 model. The data are shown by full symbols. Shadowed areas represent the systematic uncertainties. Full JM06 calculations are shown by full solid lines. The contributions from N^*'s and nonresonant mechanisms are shown by dot-dashed and dashed lines, respectively.

author (see footnote 3). In Tables IV– VII, we give examples of such partial waves at $Q^2 = 0.275$ GeV^2. The tables contain the partial waves for 4 of 12 independent helicity amplitudes for the photon helicity $\lambda_\gamma = 1$ at fixed values of Q^2 and running mass of $\pi^+ p$ system as a function of W. It shall be noted that the partial waves of $J = 1/2$ total angular momenta vanish for the helicity amplitudes corresponding to the $3/2$ total spin projections on the initial photon or the final pion momenta, as is expected from angular momentum conservation.

TABLE IV. The partial waves for coherent sum of Born and additional contact terms in $\pi^-\Delta^{++}$ channel of total angular momentum J and for helicities of the initial and final particles $\lambda_\gamma = 1, \lambda_p = 1/2$, $\lambda_\Delta = 3/2$. The amplitudes were evaluated at $Q^2 = 0.275$ GeV^2 and for running Δ mass 1.14 GeV.

W (GeV)	J	Real part for T^J Born and contact terms	Imaginary part for T^J Born and contact terms
1.31	0.5	0	0
1.34	0.5	0	0
1.36	0.5	0	0
1.39	0.5	0	0
1.41	0.5	0	0
1.44	0.5	0	0
1.46	0.5	0	0
1.49	0.5	0	0
1.51	0.5	0	0
1.54	0.5	0	0
1.56	0.5	0	0
1.31	1.5	−14.63	−5.31
1.34	1.5	−14.89	−5.42
1.36	1.5	−15.04	−5.48
1.39	1.5	−14.70	−5.48
1.41	1.5	−13.82	−5.45
1.44	1.5	−11.38	−5.38
1.46	1.5	−10.15	−5.28
1.49	1.5	−10.56	−5.16
1.51	1.5	−9.23	−5.00
1.54	1.5	−8.69	−4.83
1.56	1.5	−8.09	−4.64
1.31	2.5	−3.59	−0.58
1.34	2.5	−5.05	−0.87
1.36	2.5	−6.22	−1.14
1.39	2.5	−7.13	−1.39
1.41	2.5	−7.78	−1.63
1.44	2.5	−7.95	−1.87
1.46	2.5	−8.21	−2.09
1.49	2.5	−8.76	−2.31
1.51	2.5	−8.77	−2.51
1.54	2.5	−8.90	−2.70
1.56	2.5	−8.93	−2.88

TABLE V. The partial waves for coherent sum of Born and additional contact terms in $\pi^-\Delta^{++}$ channel of total angular momentum J and for helicities of the initial and final particles $\lambda_\gamma = 1, \lambda_p = 1/2$, $\lambda_\Delta = 1/2$. The amplitudes were evaluated at $Q^2 = 0.275$ GeV^2 and for running Δ mass 1.14 GeV.

W (GeV)	J	Real part for T^J Born and contact terms	Imaginary part for T^J Born and contact terms
1.31	0.5	−0.09	0.73
1.34	0.5	−0.12	1.04
1.36	0.5	1.25	1.28
1.39	0.5	1.36	1.47
1.41	0.5	2.18	1.63
1.44	0.5	3.19	1.76
1.46	0.5	3.63	1.85
1.49	0.5	3.72	1.92
1.51	0.5	4.65	1.97
1.54	0.5	4.73	1.98
1.56	0.5	4.52	1.98
1.31	1.5	−12.56	−4.37
1.34	1.5	−11.99	−4.05
1.36	1.5	−11.25	−3.74
1.39	1.5	−10.41	−3.42
1.41	1.5	−8.99	−3.09
1.44	1.5	−6.18	−2.76
1.46	1.5	−4.60	−2.41
1.49	1.5	−4.60	−2.07
1.51	1.5	−2.80	−1.72
1.54	1.5	−2.04	−1.37
1.56	1.5	−1.40	−1.03
1.31	2.5	−3.86	−0.62
1.34	2.5	−5.16	−0.89
1.36	2.5	−6.05	−1.12
1.39	2.5	−6.67	−1.33
1.41	2.5	−6.96	−1.51
1.44	2.5	−6.69	−1.68
1.46	2.5	−6.53	−1.83
1.49	2.5	−6.71	−1.96
1.51	2.5	−6.23	−2.07
1.54	2.5	−5.96	−2.15
1.56	2.5	−5.64	−2.20

C. Resonant mechanisms

With the parameters determined, we can examine the resonant and nonresonant contributions within JM06. The results for the integrated cross sections are already shown in Fig. 13. The results for the nine differential cross sections at $W = 1.51$ GeV and $Q^2 = 0.425$ GeV^2 are shown in Fig. 14.

In Fig. 13 we see that the contribution from resonant cross sections becomes sizable at $W > 1.40$ GeV and increases with W. The resonant contributions also increase with Q^2. At $W > 1.40$ GeV the resonant contribution ranges from 10 to 30%. In Fig. 14 we see that the shapes of the resonant and nonresonant differential cross sections are rather different, allowing us to isolate the resonant contribution in a combined fit of nine onefold differential cross sections, despite relatively small resonant contributions to the fully integrated cross sections.

From analyzing the results shown in Figs. 13 and 14, we find that the dominant part of resonant cross sections at $W < 1.6$ GeV and Q^2 from 0.25 to 0.60 GeV^2 comes from the $P_{11}(1440)$ and $D_{13}(1520)$ resonant states. Previously, the $P_{11}(1440)$ and $D_{13}(1520)$ electrocouplings at a single $Q^2 = 0.4$ GeV^2 were determined from the analysis of the 1π CLAS data [35]. The analysis presented above has extended the determination of these resonance parameters to cover the region of photon virtualities from 0.25 to 0.60 GeV^2. Moreover, in $p\pi^+\pi^-$ production the contribution from $P_{11}(1440)$ does not interfere with that from the tail of $P_{33}(1223)$ as it does in $N\pi$ electroproduction. This feature makes $p\pi^+\pi^-$

TABLE VI. The partial waves for coherent sum of Born and additional contact terms in $\pi^-\Delta^{++}$ channel of total angular momentum J and for helicities of the initial and final particles $\lambda_\gamma = 1, \lambda_p = 1/2, \lambda_\Delta = -1/2$. The amplitudes were evaluated at $Q^2 = 0.275$ GeV^2 and for running Δ mass 1.14 GeV.

W (GeV)	J	Real part for T^J Born and contact terms	Imaginary part for T^J Born and contact terms
1.31	0.5	−0.77	0.40
1.34	0.5	−1.35	0.42
1.36	0.5	−1.24	0.38
1.39	0.5	−1.23	0.31
1.41	0.5	−0.96	0.22
1.44	0.5	−0.10	0.12
1.46	0.5	0.10	0.009
1.49	0.5	0.012	−0.109
1.51	0.5	0.24	−0.22
1.54	0.5	0.12	−0.34
1.56	0.5	−0.10	−0.45
1.31	1.5	−11.00	−3.67
1.34	1.5	−10.06	−3.12
1.36	1.5	−9.21	−2.63
1.39	1.5	−8.42	−2.18
1.41	1.5	−7.27	−1.76
1.44	1.5	−4.98	−1.37
1.46	1.5	−3.77	−1.01
1.49	1.5	−3.34	−0.67
1.51	1.5	−2.77	−0.37
1.54	1.5	−2.42	−0.12
1.56	1.5	−2.14	0.11
1.31	2.5	−3.41	−0.53
1.34	2.5	−4.34	−0.72
1.36	2.5	−4.90	−0.86
1.39	2.5	−5.24	−0.98
1.41	2.5	−5.31	−1.07
1.44	2.5	−4.92	−1.13
1.46	2.5	−4.64	−1.17
1.49	2.5	−4.71	−1.20
1.51	2.5	−4.23	−1.19
1.54	2.5	−3.96	−1.15
1.56	2.5	−3.67	−1.09

TABLE VII. The partial waves for coherent sum of Born and additional contact terms in $\pi^-\Delta^{++}$ channel of total angular momentum J and for helicities of the initial and final particles $\lambda_\gamma = 1, \lambda_p = 1/2, \lambda_\Delta = -3/2$. The amplitudes were evaluated at $Q^2 = 0.275$ GeV^2 and for running Δ mass 1.14 GeV.

W (GeV)	J	Real part for T^J Born and contact terms	Imaginary part for T^J Born and contact terms
1.31	0.5	0	0
1.34	0.5	0	0
1.36	0.5	0	0
1.39	0.5	0	0
1.41	0.5	0	0
1.44	0.5	0	0
1.46	0.5	0	0
1.49	0.5	0	0
1.51	0.5	0	0
1.54	0.5	0	0
1.56	0.5	0	0
1.31	1.5	−9.82	−3.29
1.34	1.5	−8.70	−2.78
1.36	1.5	−7.97	−2.42
1.39	1.5	−7.25	−2.12
1.41	1.5	−6.44	−1.88
1.44	1.5	−4.98	−1.67
1.46	1.5	−4.16	−1.49
1.49	1.5	−4.23	−1.34
1.51	1.5	−3.47	−1.20
1.54	1.5	−3.16	−1.08
1.56	1.5	−2.85	−0.97
1.31	2.5	−2.44	−0.35
1.34	2.5	−2.95	−0.43
1.36	2.5	−3.24	−0.47
1.39	2.5	−3.37	−0.50
1.41	2.5	−3.38	−0.52
1.44	2.5	−3.16	−0.53
1.46	2.5	−3.01	−0.53
1.49	2.5	−3.04	−0.53
1.51	2.5	−2.82	−0.52
1.54	2.5	−2.70	−0.52
1.56	2.5	−2.56	−0.51

exclusive channel particularly attractive for the studies of the $P_{11}(1440)$ resonance.

VI. CONCLUSIONS AND OUTLOOK

The analysis of comprehensive CLAS data on charged double-pion electroproduction at $W < 1.6$ GeV and $Q^2 = 0.25$–0.60 GeV^2 within the framework of the JM06 model allowed us to establish all essential contributing mechanisms at those kinematics. A good description of nine onefold differential and fully integrated cross sections was achieved in the entire kinematics. The robustness of the established mechanisms was demonstrated in the successful prediction of the three angular distributions α_i $(i = 1, 2, 3)$, which were not included in the fit.

The CLAS data allowed us to evaluate the contributions from the $\pi\Delta$ channels, coherently or incoherently, to nine differential cross sections. These $\pi\Delta$ differential cross sections are determined in each bin of W and Q^2. This information as well the corresponding extracted partial wave amplitudes could be useful for a microscopic understanding of $\pi\Delta$ production mechanisms, such as that being investigated at EBAC [57–60].

Successful description within the framework of the JM06 model of the large body of $p\pi^+\pi^-$ electroproduction data allowed us to isolate the resonant parts of cross sections, offering access to electrocouplings of $P_{11}(1440)$ and $D_{13}(1520)$ resonances at $Q^2 = 0.25$–0.60 GeV^2. Evaluation of these electrocouplings is in progress [55,56]. In this low Q^2 region, the meson-baryon dressing of the N-N^* transition amplitudes is expected to be large [60,68,69]. Therefore, evolution of $P_{11}(1440)$ and $D_{13}(1520)$ electrocouplings at lower

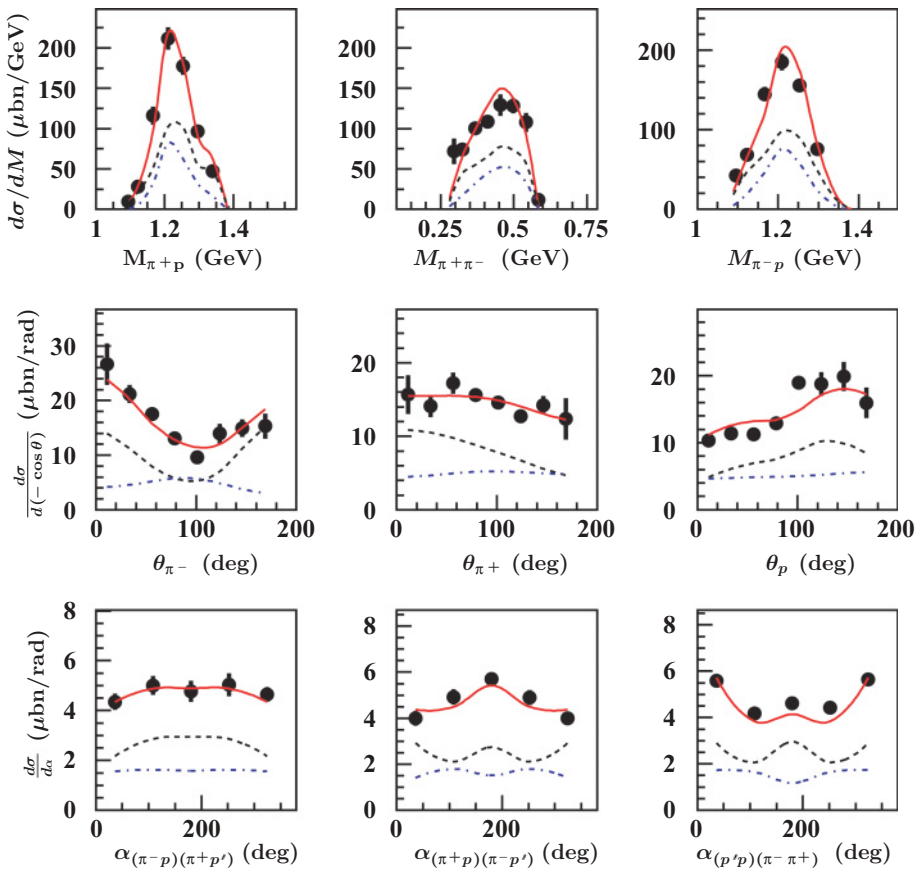

FIG. 14. (Color online) Resonant (dot-dash lines) and nonresonant (dot lines) mechanism contributions to the onefold differential cross sections at $W = 1.51$ GeV and $Q^2 = 0.425$ GeV^2. The solid lines represent the full JM06 calculation.

$Q^2 < 0.6$ GeV^2 is of particular interest for studies of meson-baryon dressing and still unexplored in double-pion electroproduction.

ACKNOWLEDGMENTS

This work was supported in part by the US Department of Energy and the National Science Foundation, the Jefferson Lab, the Argonne National Lab, the Skobeltsyn Institute of Nuclear Physics and the Physics Department at the Moscow State University, and the Russian Federation Government Grant 2009-1.1-125-055. Jefferson Science Associates, LLC, operates Jefferson Lab under US DOE Contract DE-AC05-060R23177.

APPENDIX A: BORN AMPLITUDES

Here we present the list of amplitudes for the Reggeized Born terms used in the JM06 model. These terms were derived from the diagrams shown in Fig. 15. They consist of the contact term, the t-channel pion-in-flight diagram, the s-pole nucleon term, and the u-channel Δ-in-flight diagram [39,70]. To describe the off-shell pion or Δ interactions to the hadronic currents shown in the right-side diagrams of the Fig. 15, the respective hadronic vertex functions were used. The off-shell effects in virtual photon interactions to the hadronic currents depicted in Fig. 15 were taken into account by implementing electromagnetic vertex functions. For hadronic and electromagnetic vertex functions we used a compilation of experimental data [63,71,72].

The helicity amplitudes for the contact term are given by

$$t^c_{\lambda_\Delta\lambda_\gamma\lambda_p} = g_c(Q^2,t)\bar{u}_\mu(p_2,\lambda_\Delta)u(p_1,\lambda_p)\varepsilon_\mu(q,\lambda_\gamma), \qquad \text{(A1)}$$

where p_1 and p_2 are the target proton and Δ four-momenta, q is the photon four-momentum, and u_μ, ε_μ, and u are Rarita-Schwinger spinor-tensor for Δ with λ_Δ helicity, the four-vector of in-going photon with λ_γ helicity, and the proton target spinor of λ_p helicity; $g_c(Q^2,t)$ is an effective contact term vertex function.

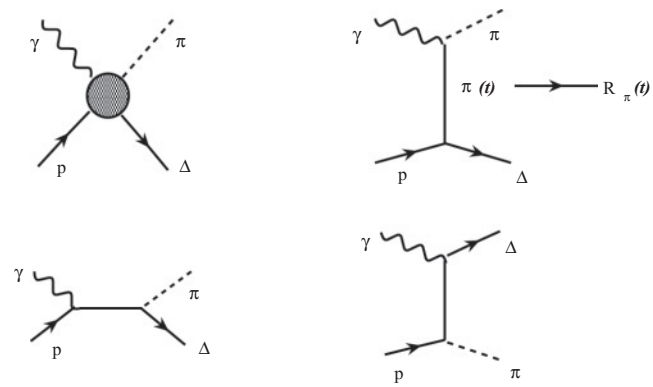

FIG. 15. Born amplitudes in JM06 model.

The pion-in-flight contribution reads:

$$t^{\rm pif}_{\lambda_\Delta\lambda_\gamma\lambda_p} = g_\pi(Q^2,t)\frac{(2p_\pi^\mu - q^\mu)\varepsilon_\mu(q,\lambda_\gamma)}{t-m_\pi^2} \times \overline{u}_\nu(p_2,\lambda_\Delta)u(p_1,\lambda_p)\big(q^\nu - p_\pi^\nu\big), \quad \text{(A2)}$$

where p_π is the pion momentum, m_π is the pion mass, and $g_\pi(Q^2,t)$ is the product of strong and electromagnetic vertex functions:

$$g_\pi(Q^2,t) = G_{\pi,\rm em}(Q^2)G_{\pi N\Delta}(t). \quad \text{(A3)}$$

The electromagnetic vertex function is described by the pole fit of the pion form factor [63]:

$$G_{\pi,\rm em}(Q^2) = \frac{1}{\left[1+\frac{Q^2({\rm GeV}^2)}{\Lambda_\pi^2}\right]}\frac{1}{G_{\pi N\Delta}(t_{\rm min})}, \quad \text{(A4)}$$

where $t_{\rm min}$ corresponds to pion production in hadronic center-of-mass at zero degree angle; the factor $\frac{1}{G_{\pi N\Delta}(t_{\rm min})}$ reflects the way $G_{\pi,\rm em}(Q^2)$ form factor was extracted from single pion electroproduction data [72]. The analysis in Ref. [72] yielded $\Lambda_\pi^2 = 0.462{\rm GeV}^2$, which we used in our calculations. Concerning the t dependence of $\pi N\Delta$ vertex, we introduce as vertex function the hadronic form factor successfully applied in $NN \to N\Delta$ relativistic transition potentials [71]:

$$G_{\pi N\Delta}(t) = g_0\frac{\Lambda^2 - m_\pi^2}{\Lambda^2 - t}. \quad \text{(A5)}$$

The interaction constant g_0 and cut-off parameter Λ are $g_0 = 2.1/m_\pi$ and $\Lambda = 0.75$ GeV. Current conservation implies equality of the contact term coupling $g_c(Q^2,t)$ and the product of the hadronic and electromagnetic vertex functions $g_\pi(Q^2,t)$ in the pion-in-flight term.

The s-channel nucleon contribution is given by:

$$t^N_{\lambda_\Delta\lambda_\gamma\lambda_p} = g_N(Q^2)g_0\frac{(2p_1^\mu + q^\mu)\varepsilon_\mu(q,\lambda_\gamma)}{s-m_N^2} \times \overline{u}_\nu(p_2,\lambda_\Delta)u(p_1,\lambda_p)p_\pi^\nu, \quad \text{(A6)}$$

where s is Mandelstam invariant $s = (q+p_1)^2$, m_N is the nucleon mass, g_N is the electromagnetic vertex function, described by the dipole fit [63]:

$$g_N(Q^2) = \frac{1}{\left[1+\frac{Q^2({\rm GeV}^2)}{0.71}\right]^2}. \quad \text{(A7)}$$

The last contribution to the Born terms that we considered was the Δ-in-flight, which is given by

$$t^\Delta_{\lambda_\Delta\lambda_\gamma\lambda_p} = 2g_\Delta(Q^2,t)\frac{(2p_2^\mu - q^\mu)\varepsilon_\mu(q,\lambda_\gamma)}{u-m_\Delta^2} \times \overline{u}_\nu(p_2,\lambda_\Delta)p_\pi^\nu u(p_1,\lambda_p), \quad \text{(A8)}$$

where u is the Mandelstam variable corresponding to the crossed invariant momentum transfer $u = (p_1 - p_\pi)^2$ and $g_\Delta(Q^2,t)$ is the product of electromagnetic and strong vertex functions. The vertex function $g_\Delta(Q^2,t)$ is related to the $g_\pi(Q^2,t)$ and g_N vertex functions by current conservation of the total Born amplitude:

$$g_\Delta(Q^2,t) = \frac{g_\pi(Q^2,t) + g_N(Q^2)}{2}. \quad \text{(A9)}$$

Finally we substituted π propagator in the pion-in-flight diagram (right top Fig. 15) by the π-Regge trajectory, following to the approach proposed in [73]:

$$\frac{1}{t-m_\pi^2} \to R_\pi(t) = \left(\frac{S}{S_0}\right)^{\alpha_\pi(t)}\frac{\pi\alpha'_\pi}{\sin[\pi\alpha_\pi(t)]} \times \frac{1+e^{-i\pi\alpha_\pi(t)}}{2} \times \frac{1}{\Gamma[1+\alpha_\pi(t)]} \quad \text{(A10)}$$

where $S_0 = 1.0$ GeV^2, $\alpha' = 0.7$ GeV^{-2} is the slope of the pion Regge trajectory, and Γ is the γ function. The pion Regge trajectory $\alpha_\pi(t)$ is given by

$$\alpha_\pi(t) = \alpha'\big(t - m_\pi^2\big), \quad \text{(A11)}$$

where the dimension variables are in units of GeV^2. We also implemented an additional W-independent multiplicative factor α_R to the Reggeized t-channel Born amplitudes to account for the differences in effective electromagnetic and hadronic couplings for Regge trajectory and for the pion. Parameter α_R was determined from the data fit and is equal to 1.35.

Reggeized Born terms were obtained by multiplying all Born amplitudes with a common factor:

$$\alpha_R\big(t - m_\pi^2\big)R_\pi(t). \quad \text{(A12)}$$

In this way we maintain the full Reggeized Born amplitude, which remains current conserving, while the t-channel term acquires the propagator $R_\pi(t)$ Eq. (A10), instead of the pion pole.

APPENDIX B: THE AMPLITUDES FOR NONRESONANT MECHANISMS IN $\pi\Delta$ CHANNELS BEYOND REGGEIZED BORN TERMS

Here we present the expressions for nonresonant mechanisms in $\pi\Delta$ channels, complementary to the Reggeized Born terms, described in Appendix A. These mechanisms were parametrized by two additional contact terms:

$$t^c = \big[A(W,Q^2)\epsilon_\mu^\gamma\overline{u}_\Delta^\nu\gamma^\mu u p_\nu^\pi + B(W,Q^2)\epsilon_\nu^\gamma\overline{u}_\Delta^\nu\gamma^\delta u(2p_\pi - q_\gamma)_\delta\big]\frac{1}{t-\Lambda^2}. \quad \text{(B1)}$$

Parameters $A(W,Q^2)$, $B(W,Q^2)$ were fitted to the CLAS data in each bin of W and Q^2 independently. The factor $\frac{1}{t-\Lambda^2}$ in Eq. (B1) allowed us to better describe the angular distributions of the final hadrons. The cut-off parameter Λ^2 was determined to 1.64 GeV^2 from the data fit.

These terms could effectively account for the additional contributions to the $\pi\Delta$ final states from other open exclusive channels arising from hadronic final-state interactions. These

TABLE VIII. The parameters $A(W, Q^2)$, $B(W, Q^2)$ in Eq. (B1) derived from the CLAS data fit at $Q^2 = 0.275$ GeV^2

W (GeV)	$A(W,Q^2)$, GeV $\pi^-\Delta^{++}$ channel	$B(W,Q^2)$, GeV $\pi^-\Delta^{++}$ channel	$A(W,Q^2)$, GeV $\pi^+\Delta^0$ channel	$B(W,Q^2)$, GeV $\pi^+\Delta^0$ channel
1.31	7.0	63.0	5.0	45.0
1.34	4.5	40.5	5.0	50.0
1.36	22.5	22.5	17.0	17.0
1.39	22.5	22.5	30.0	30.0
1.41	15.0	10.0	36.0	24.0
1.44	16.0	4.0	62.4	15.6
1.46	18.0	2.0	90.0	10.0
1.49	14.4	3.6	88.0	12.0
1.51	9.0	1.0	126.0	14.0
1.54	7.2	0.8	126.0	14.0
1.56	5.4	0.6	128.0	14.5

extra terms may come from other mechanisms in $\pi\Delta$ production in addition to Reggeized Born terms. Lorentz structure of the transition $p \to \Delta$ current could be more complex than a simple tensor structure $g_{\mu\nu}$, which was used for the Reggeized Born terms of Appendix A. The two terms in Eq. (B1) may originate from the additional tensor structures, which may enter into this current:

$$\gamma^\mu p_\nu^\pi, \qquad p_c^\delta \gamma_\delta g_{\mu\nu}, \tag{B2}$$

where $p_c = (2p_\pi - q_\gamma)$ is the difference of the final pion momentum and momentum transferred $q_\gamma - p_\pi$. The tensor structures (B2) being contracted to the spin tensors of the initial and the final particles gives us the first and the second terms in Eq. (B1), respectively. We found no evidence for contributions to the $p \to \Delta$ transition current from other tensor structures.

The parameters $A(W, Q^2)$, $B(W, Q^2)$ in Eq. (B1), obtained from the CLAS data fit, are listed in the Tables VIII–XIV for both $\pi^-\Delta^{++}$ and $\pi^+\Delta^0$ isobar channels. In the fits we varied sum of $A(W, Q^2)$ and $B(W, Q^2)$, while their ratio was fixed in preliminary adjustment to the CLAS data [10].

TABLE IX. The parameters $A(W, Q^2)$, $B(W, Q^2)$ in Eq. (B1) derived from the CLAS data fit at $Q^2 = 0.325$ GeV^2

W (GeV)	$A(W,Q^2)$, GeV $\pi^-\Delta^{++}$ channel	$B(W,Q^2)$, GeV $\pi^-\Delta^{++}$ channel	$A(W,Q^2)$, GeV $\pi^+\Delta^0$ channel	$B(W,Q^2)$, GeV $\pi^+\Delta^0$ channel
1.31	8.0	72.0	3.7	33.3
1.34	9.6	86.4	6.0	54.0
1.36	25.0	25.0	77.5	77.5
1.39	20.0	20.0	75.0	75.0
1.41	28.0	12.0	80.5	34.5
1.44	56.0	14.0	92.0	23.0
1.46	56.0	14.0	104.0	11.0
1.49	20.0	5.0	100.0	25.0
1.51	12.0	3.0	135.0	15.0
1.54	12.0	3.0	153.0	17.0

TABLE X. The parameters $A(W, Q^2)$, $B(W, Q^2)$ in Eq. (B1) derived from the CLAS data fit at $Q^2 = 0.375$ GeV^2

W (GeV)	$A(W,Q^2)$, GeV $\pi^-\Delta^{++}$ channel	$B(W,Q^2)$, GeV $\pi^-\Delta^{++}$ channel	$A(W,Q^2)$, GeV $\pi^+\Delta^0$ channel	$B(W,Q^2)$, GeV $\pi^+\Delta^0$ channel
1.31	7.0	63.0	3.7	33.3
1.34	8.0	72.0	6.0	54.0
1.36	29.0	29.0	35.0	35.0
1.39	25.0	25.0	25.0	25.0
1.41	33.6	14.4	21.0	10.0
1.44	40.0	10.0	32.0	8.0
1.46	22.5	2.5	45.5	5.0
1.49	16.0	4.0	56.0	14.0
1.51	16.0	4.0	81.0	9.0
1.54	16.0	4.0	108.0	12.0

APPENDIX C: FULL THREE-BODY AMPLITUDES FOR ISOBAR CHANNELS

The three-body amplitudes for $\gamma p \to \pi\Delta \to p\pi^+\pi^-$ isobar channels $T^{\pi\Delta}_{\gamma^* N,\pi\pi N}$ [Eq. (1)] were calculated using a Breit-Wigner ansatz as a product of quasi-two-body $\pi\Delta$ production amplitudes $\langle \pi\lambda_\Delta | T | \lambda_p \lambda_\gamma \rangle$, shown in square brackets in Eq. (2); $\Delta \to \pi N \langle \pi\lambda_{p'} | T | \lambda_\Delta \rangle$ decay amplitudes [$\Gamma_{\Delta,\pi N}$ in Eq. (2)]; and Δ propagator [G_Δ in Eq. (2)]:

$$T^{\pi\Delta}_{\gamma^* N,\pi\pi N} = \sum_{\lambda_\Delta} \frac{\langle \pi\lambda_{p'} | T | \lambda_\Delta \rangle \langle \pi\lambda_\Delta | T | \lambda_p \lambda_\gamma \rangle}{M_\Delta^2 - M_{\pi p}^2 - i\Gamma_\Delta(M_{\pi p}) M_\Delta}, \tag{C1}$$

where M_Δ, $\Gamma_\Delta(M_{\pi p})$ are the Δ mass and total hadronic decay width, which is a function of running $M_{\pi p}$ masses. The mass dependence was obtained by calculating the total decay width $\Gamma_\Delta(M_{\pi p})$ from the matrix elements (C2). Therefore, expression Eq. (C1) fulfills the unitarity conditions. The sum is running over helicities λ_Δ.

The $\langle \pi\lambda_{p'} | T | \lambda_\Delta \rangle$ decay amplitudes were calculated as:

$$\langle \pi\lambda_{p'} | T | \lambda_\Delta \rangle = g_\Delta F_\Delta(M_{\pi p}) \bar{u}_{p'} u^\mu_\Delta p^\pi_\mu, \tag{C2}$$

TABLE XI. The parameters $A(W, Q^2)$, $B(W, Q^2)$ in Eq. (B1) derived from the CLAS data fit at $Q^2 = 0.425$ GeV^2.

W (GeV)	$A(W,Q^2)$, GeV $\pi^-\Delta^{++}$ channel	$B(W,Q^2)$, GeV $\pi^-\Delta^{++}$ channel	$A(W,Q^2)$, GeV $\pi^+\Delta^0$ channel	$B(W,Q^2)$, GeV $\pi^+\Delta^0$ channel
1.31	9.8	88.2	3.7	33.3
1.34	8.4	75.6	4.0	36.0
1.36	55.0	55.0	30.0	30.0
1.39	53.0	53.0	20.0	20.0
1.41	80.6	34.5	21.0	9.0
1.44	80.0	20.0	24.0	6.0
1.46	54.0	6.0	45.0	5.0
1.49	38.4	9.6	32.0	8.0
1.51	18.0	2.0	26.0	4.0

TABLE XII. The parameters $A(W,Q^2)$, $B(W,Q^2)$ in Eq. (B1) derived from the CLAS data fit at $Q^2 = 0.475$ GeV^2.

W (GeV)	$A(W,Q^2)$, GeV $\pi^-\Delta^{++}$ channel	$B(W,Q^2)$, GeV $\pi^-\Delta^{++}$ channel	$A(W,Q^2)$, GeV $\pi^+\Delta^0$ channel	$B(W,Q^2)$, GeV $\pi^+\Delta^0$ channel
1.31	14.5	131.5	7.7	69.3
1.34	10.0	90.0	7.5	67.5
1.36	55.0	55.0	70.0	70.0
1.39	45.0	45.0	55.0	55.0
1.41	91.0	39.0	91.0	39.0
1.44	80.0	20.0	96.0	24.0
1.46	45.0	5.0	90.0	10.0
1.49	16.0	4.0	48.0	12.0

The coupling constant g_Δ, was fitted to the total hadronic decay widths of the Δ at the central mass 1.23 GeV:

$$g_{\Delta^{++}\to\pi^+ p} = 15, \tag{C3}$$

$$g_{\Delta^{+}\to\pi^- p} = 15 * (1/\sqrt{3}). \tag{C4}$$

A numerical factor $1/\sqrt{3}$ represents isospin Clebsch-Gordan coefficient.

Mass dependence of the total hadronic decay widths $\Gamma_\Delta(M_{\pi p})$ was determined through the Lorentz structure of decay amplitudes (C2), as well as the hadronic form factors $F_\Delta(M_{\pi p})$ [74]:

$$F_\Delta(M_{\pi p}) = \frac{F(P^*_{\pi R})}{F(P^*_\pi)}, \qquad F(P^*_\pi) = \sqrt{\frac{P^{*2}_\pi}{\Lambda^2_\Delta + P^{*2}_\pi}}\left\{\frac{P^*_{\pi R}}{P^*_\pi}\right\}, \tag{C5}$$

where P^*_π, $P^*_{\pi R}$ are moduli of pion three-momenta in the rest frame of the Δ at current and the central $M_{\pi p}$, respectively. $\Lambda_\Delta = 0.235$ GeV.

TABLE XIII. The parameters $A(W,Q^2)$, $B(W,Q^2)$ in Eq. (B1) derived from the CLAS data fit at $Q^2 = 0.525$ GeV^2.

W (GeV)	$A(W,Q^2)$, GeV $\pi^-\Delta^{++}$ channel	$B(W,Q^2)$, GeV $\pi^-\Delta^{++}$ channel	$A(W,Q^2)$, GeV $\pi^+\Delta^0$ channel	$B(W,Q^2)$, GeV $\pi^+\Delta^0$ channel
1.31	8.5	76.5	7.7	69.3
1.34	8.0	80.0	7.5	67.5
1.36	90.0	90.0	60.0	60.0
1.39	75.0	75.0	50.0	50.0
1.41	87.5	37.5	91.0	39.0
1.44	88.0	22.0	104.0	26.0
1.46	81.0	9.0	99.0	9.0
1.49	30.4	7.6	38.4	9.6

TABLE XIV. The parameters $A(W,Q^2)$, $B(W,Q^2)$ in Eq. (B1) derived from the CLAS data fit at $Q^2 = 0.575$ GeV^2.

W (GeV)	$A(W,Q^2)$, GeV $\pi^-\Delta^{++}$ channel	$B(W,Q^2)$, GeV $\pi^-\Delta^{++}$ channel	$A(W,Q^2)$, GeV $\pi^+\Delta^0$ channel	$B(W,Q^2)$, GeV $\pi^+\Delta^0$ channel
1.31	7.5	67.5	4.7	42.3
1.34	6.8	61.2	7.5	67.5
1.36	80.0	80.0	60.0	60.0
1.39	75.0	75.0	55.0	55.0
1.41	84.0	36.0	91.0	39.0
1.44	96.0	24.0	104.0	26.0

APPENDIX D: CROSS SECTIONS AND AMPLITUDES IN THE JM06 MODEL

All amplitudes were calculated for the S matrix defined as:

$$S = I + (2\pi)^4\delta^4(P_f - P_i)iT, \tag{D1}$$

where P_f and P_i are total four-momenta of the final and the initial particles, respectively. The Dirac spinors were normalized as

$$\overline{U_p}U_p = 2M_N, \tag{D2}$$

where U_p, $(\overline{U_p})$ are Dirac (conjugated Dirac) spinors and M_N is the nucleon mass. With this parametrization of the S-matrix and Dirac spinor normalization, the phase-space element for the final particle i with three-momentum vector $\vec{p}_i$ and energy E_i is defined as

$$d^3\vec{p}_i/[2E_i(2\pi)^3], \tag{D3}$$

All time-space tensors (currents, the particle four-momenta) in the JM model correspond to the $g_{\mu\nu}$ tensor ($\mu = 0, 1, 2, 3, 4$) with the components: $g_{00} = 1$, $g_{11} = g_{22} = g_{33} = -1$.

The cross sections of $p\pi^+\pi^-$ exclusive reaction induced by virtual photons absorption off the protons were determined in the single-photon-exchange approximation. These cross sections are related to the measured exclusive electron scattering cross sections according to Eq. (3) of Sec. II. This formalism is described in details in Ref. [63]. The kinematics of the $p\pi^+\pi^-$ final state are determined unambiguously by the fivefold differential cross section $d^5\sigma$ (see Sec. II). This fivefold differential cross section for $p\pi^+\pi^-$ production by virtual photons off the protons was calculated as a contraction of leptonic and hadronic tensors divided by the invariant virtual photon flux and multiplied by the $d^5\Phi$ phase-space differential for the three-body final state. The leptonic tensor $L_{\mu\nu}$ is well known from QED [63]. The hadronic tensor represents a product of the hadronic currents J^*_μ and J_ν contracted to the spin-density matrices for the initial and the final hadrons.

This article deals with spin-averaged differential cross sections that are independent of any polarization observable. The $d^5\sigma$ cross section is computed for unpolarized electron beam, proton target, and with the unity spin-density matrices for the final-state hadrons. To get rid of the virtual photon polarization degree of freedom, we integrate the $d^5\sigma$ cross section over the azimuthal ϕ angle of one of the final hadrons,

defined in Sec. II. This integration results in a ϕ-independent fourfold differential cross section.

The fourfold differential $\gamma_{\rm virt} p \to p\pi^+\pi^-$ cross section after integration over the final π^- azimuthal angle ϕ_{π^-} is given by:

$$d^4\sigma = \frac{4\pi\alpha}{4K_L M_N}\left\{\frac{J_x^* J_x + J_y^* J_y}{2} + \epsilon_L J_z^* J_z\right\} d^4\phi, \qquad \text{(D4)}$$

where α is fine structure constant and ϵ_L stands for degree of longitudinal polarization of virtual photons, as it was defined in Ref. [63]. The factor $4K_L M_N$ is the invariant virtual photon flux, M_N is nucleon mass, K_L is the equivalent photon energy:

$$K_L = \frac{W^2 - M_N^2}{2M_N}, \qquad \text{(D5)}$$

$d^4\phi$ stands for the three-body phase-space differential after integration over ϕ_{π^-}. This differential may be expressed in terms of the final-state kinematic variables as:

$$\begin{aligned} d^4\phi &= 2\pi\frac{1}{32W^2(2\pi)^5} ds_{\pi^+\pi^-} ds_{\pi^+ p} d\theta_{\pi^-} d\alpha_{[p'\pi^+][p\pi^-]}, \\ ds_{\pi^+\pi^-} &= dM^2_{\pi^+\pi^-}, \\ ds_{\pi^+ p} &= dM^2_{\pi^+ p}, \end{aligned} \qquad \text{(D6)}$$

where W is invariant mass of the final hadron system, while the M_{ij} are the invariant masses of the i, j pair of the final hadrons. All angles for the final hadrons are defined in the hadronic center-of-mass frame (see Sec. II for definition of kinematic variables).

The Eq. (D4) also gives the onefold differential cross sections for isobar channels $\gamma p \to \pi\Delta$ with the unstable final particle Δ of running mass M_Δ. To get these cross sections, $d^4\phi$ differential in Eq. (D4) should be replaced by onefold differential $\mathrm{d}\Phi_{2b}$ describing phase space element for two-body final state after integration over the final hadron ϕ angle:

$$d\Phi_{2b} = 2\pi\frac{p_f}{4W} d\theta_f, \qquad \text{(D7)}$$

$$E_f = \frac{W^2 + M_f^2 - M_{f'}^2}{2W}, \qquad \text{(D8)}$$

$$p_f = \sqrt{E_f^2 - M_f^2}, \qquad \text{(D9)}$$

where E_f, P_f are the energy and momentum modules of one of the final hadron f ($f = \pi, \Delta$), M_f is its mass, while the index f' stands for the other hadron. All frame-dependent kinematic variables of the final hadrons are defined in the $\pi\Delta$ or $\gamma_{\rm virt} p$ center-of-mass frame.

The longitudinal polarization parameter ϵ_L of the virtual photon is determined by the electron electromagnetic currents. The QED calculations give [63]:

$$\epsilon_L = \sqrt{\frac{Q^2}{\nu^2}}\left\{1 + 2\frac{Q^2 + \nu^2}{Q^2} tg^2\frac{\theta_{e'}}{2}\right\}^{-1}, \qquad \text{(D10)}$$

where ν is Lorentz invariant in electron scattering:

$$\nu = \frac{(qp)}{M_N}, \qquad \text{(D11)}$$

and q and p are the four-momenta of photon and target proton, respectively. The ν value is equal to the energy transferred to the virtual photon in the laboratory frame. $\theta_{e'}$ is the electron scattering angle in the laboratory frame.

The hadronic current J_ν and the virtual photon vectors $\epsilon(\lambda_\gamma)$ ($\lambda_\gamma = -1, 0, +1$) are related to reaction helicity amplitudes $\langle\lambda_f|T|\lambda_p\lambda_\gamma\rangle$ as:

$$\epsilon_\nu(\lambda_\gamma = -1) J^\nu(\lambda_p, \lambda_f) = \langle\lambda_f|T|\lambda_p\lambda_\gamma = -1\rangle, \qquad \text{(D12)}$$

$$\epsilon_\nu(\lambda_\gamma = 1) J^\nu(\lambda_p, \lambda_f) = \langle\lambda_f|T|\lambda_p\lambda_\gamma = 1\rangle, \qquad \text{(D13)}$$

$$\epsilon_\nu(\lambda_\gamma = 0) J^\nu(\lambda_p, \lambda_f) = \langle\lambda_f|T|\lambda_p\lambda_\gamma = 0\rangle, \qquad \text{(D14)}$$

where λ_i ($i = \gamma, p$) stand for the initial-state photon and proton helicities. The λ_f is generic symbol for the helicities in the final state. The vectors $\epsilon(\lambda_\gamma)$ were estimated in the laboratory frame in all JM calculations, resulting in the hadronic currents and hadronic tensor determined in laboratory frame.[4] Contracted components of the leptonic and the hadronic tensors should be determined in the same frame. Therefore, components of the leptonic tensor should calculated in the laboratory frame. This is a reason why the kinematical variables in Eq. (D10) were evaluated in the laboratory frame.

The J_0 component of the hadronic current was obtained employing current conservation:

$$q_0 J^0 - q_z J^z = 0. \qquad \text{(D15)}$$

The hadronic currents J_ν were derived from Eqs. (D12)–(D15):

$$\begin{aligned} J_x &= -\frac{\langle\lambda_f|T|\lambda_p\lambda_\gamma = 1\rangle - \langle\lambda_f|T|\lambda_p\lambda_\gamma = -1\rangle}{\sqrt{2}}, \\ J_y &= i\frac{\langle\lambda_f|T|\lambda_p\lambda_\gamma = 1\rangle + \langle\lambda_f|T^|\lambda_p\lambda_\gamma = -1\rangle}{\sqrt{2}}, \\ J_z &= \frac{\nu}{\sqrt{Q^2}}\langle\lambda_f|T|\lambda_p\lambda_\gamma = 0\rangle. \end{aligned} \qquad \text{(D16)}$$

Because the contraction of the leptonic and the hadronic tensors is Lorentz invariant, all expressions for cross sections listed above are valid in any frame. However, the expressions for Lorentz invariants in cross sections incorporate the frame-dependent observables defined in particular frames: electron scattering angle in the laboratory frame and the final hadron angles in the center-of-mass frame.

APPENDIX E: PARAMETERS FOR THE RESONANT MECHANISMS

Here we present the initial values of the parameters of $P_{11}(1440)$ and $D_{13}(1520)$ resonances used in computing the various isobar channel contributions. They were obtained from interpolation of previously available CLAS/world N^*

[4] Explicit expressions for the photon vectors $\epsilon_\nu(\lambda_\gamma)$ may be found in Ref. [63].

TABLE XV. The initial values of $P_{11}(1440)$ and $D_{13}(1520)$ electrocouplings used in calculations of the contributions from various isobar channels.

Q^2 (GeV^2)	P_{11} (1440) $A_{1/2}\times 10^3$ (GeV$^{-1/2}$)	P_{11} (1440) $S_{1/2}\times 10^3$ (GeV$^{-1/2}$)	D_{13} (1520) $A_{1/2}\times 10^3$ (GeV$^{-1/2}$)	D_{13} (1520) $S_{1/2}\times 10^3$ (GeV$^{-1/2}$)	D_{13} (1520) $A_{3/2}\times 10^3$ (GeV$^{-1/2}$)
0.275	−33.0	50.0	−55.0	−47.0	70.0
0.325	−25.0	51.0	−58.0	−50.0	70.0
0.375	−15.0	36.0	−65.0	−62.0	80.0
0.425	0.0	43.0	−80.0	−48.0	70.0
0.475	17.0	44.0	−65.0	−48.0	70.0
0.525	20.0	45.0	−60.0	−48.0	70.0
0.575	27.0	46.0	−55.0	−48.0	63.0

electrocoupling data [66] to the kinematical area covered by the recent CLAS data [10]. The starting values of hadronic parameters were taken from previous analysis of the CLAS $N\pi\pi$ electroproduction data within the framework of JM05 model [52]. Interpolated electrocoupling values were further adjusted to measured differential cross sections. Only those resonances listed in Tables XV and XVI have a measurable impact on observables in the CLAS data. The contributions from other resonances are well inside the data uncertainties. Listed in the Tables XV and XVI resonance parameters were varied as described in Sec. IV.

These parameters should be used in combination with nonresonant JM06 parameters to describe superposition of resonant and nonresonant mechanisms in various isobar channels. They cannot be interpreted as resonance parameter values derived from the data fit, because no attempt was made to improve the determined N^* parameters as well as to evaluate the uncertainties of N^* parameters, related to the accuracies of measured cross sections.

APPENDIX F: THE SET OF PARTIAL WAVES USED FOR EXPANSION OF THE NONRESONANT HELICITY AMPLITUDES IN $\pi\Delta$ ISOBAR CHANNELS

Nonresonant helicity amplitudes in $\pi\Delta$ isobar channels were expanded over the set of partial waves, corresponding to the quantum states with the total angular momenta J and its projections μ and ν onto the directions along the initial and final particle momenta in the center-of-mass frame. The defined partial waves $\langle\pi\lambda_\Delta|T^J|\lambda_\gamma\lambda_p\rangle$ are related to the full helicity amplitude $\langle\pi\lambda_\Delta|T|\lambda_\gamma\lambda_p\rangle$ as:

$$\langle\pi\lambda_\Delta|T^J|\lambda_\gamma\lambda_p\rangle = \int_0^\pi \frac{2J+1}{2}\langle\pi\lambda_\Delta|T|\lambda_\gamma\lambda_p\rangle \times d^J_{\mu\nu}(\cos\theta_\pi)\sin\theta_\pi d\theta_\pi$$
$$\mu = \lambda_\gamma - \lambda_p$$
$$\nu = -\lambda_\Delta. \quad \text{(F1)}$$

The helicity amplitudes $\langle\pi\lambda_\Delta|T|\lambda_\gamma\lambda_p\rangle$ may be written as infinite sums over the partial waves in Eq. (F1)

$$\langle\pi\lambda_\Delta|T|\lambda_\gamma\lambda_p\rangle = \sum_J \langle\pi\lambda_\Delta|T^J|\lambda_\gamma\lambda_p\rangle d^J_{\mu\nu}(\cos\theta_\pi), \quad \text{(F2)}$$

where θ_π is the pion polar emission angle in the center-of-mass frame. CLAS data analysis showed that at $W < 1.55$ GeV the partial wave basis may be restricted to $J_{\max} = 5/2$. Contribution from partial waves with $J > 5/2$ are inside the data uncertainties.

The helicity amplitudes depend on the W, Q^2 variables, describing the initial state and on the θ_π, $M_{\pi p}$ variables of the final state, where $M_{\pi p}$ stands for running mass of the Δ isobar. After integration (F1) the partial waves $\langle\pi\lambda_\Delta|T^J|\lambda_\gamma\lambda_p\rangle$ depend on the W, Q^2, and $M_{\pi p}$ variables only. All helicity amplitudes and partial waves, discussed here, contain the factor $e^{i(\lambda_\gamma-\lambda_p)\phi_\pi}$, which describes their dependence on the pion azimuthal emission angle ϕ_π. This exponential factor is retained for any reaction dynamic, being a consequence of the rotational invariance of the production amplitudes.

Instead of helicity representation, LS representation is frequently used for the description of the $\pi\Delta$ final state. The partial waves $\langle\pi\lambda_\Delta|T^J|\lambda_\gamma\lambda_p\rangle$ in helicity representation may be expressed through the partial waves $\langle LS(\pi\Delta)|T^J|\lambda_\gamma\lambda_p\rangle$, in LS representation as

$$\langle\pi\lambda_\Delta|T|\lambda_\gamma\lambda_p\rangle = \sum_{LS}\langle\pi\lambda_\Delta|LS\rangle\langle LS(\pi\Delta)|T^J|\lambda_\gamma\lambda_p\rangle. \quad \text{(F3)}$$

The transition coefficients $\langle\pi\lambda_\Delta|LS\rangle$ are given by the products of Clebsch-Gordan coefficients and the factor accounting for different wave function normalizations in the LS and helicity representations

$$\langle LS|\pi\lambda_\Delta\rangle = \sqrt{\frac{2J+1}{2L+1}}\langle L0S = 3/2-\lambda_\Delta|J-\lambda_\Delta\rangle \times\langle 0\ 0\ 3/2-\lambda_\Delta|S-\lambda_\Delta\rangle. \quad \text{(F4)}$$

The Clebsch-Gordan coefficient $\langle S_\pi = 0, \lambda_\pi = 0, S_\Delta = 3/2, -\lambda_\Delta|S = 3/2, -\lambda_\Delta\rangle$ describes the spinless π and the Δ of 3/3 spin, which are coupled to the total spin $S = 3/2$. Because the quantization axis is along the π momenta, the total spin projection is $-\lambda_\Delta$. The Clebsch-Gordan coefficient $\langle L0S-\lambda_\Delta|J-\lambda_\Delta\rangle$ corresponds to the orbital angular momentum L and the total spin $S = 3/2$ of the $\pi\Delta$ system coupled to the total angular momentum J. The projection of the orbital angular momentum is equal to zero because of the choice of the quantization axis mentioned above.

TABLE XVI. The $P_{11}(1440)$ and $D_{13}(1520)$ hadronic decay widths used to extract contributions from different isobar channels.

	P_{11} (1440)	D_{13} (1520)
Γ_{tot} (MeV)	320	125
$\Gamma_{\pi\Delta}$ (MeV)	77	29
$\Gamma_{\rho p}$ (MeV)	0	11

[1] K. Joo *et al.* (CLAS Collaboration), Phys. Rev. Lett. **88**, 122001 (2002).
[2] K. Joo *et al.* (CLAS Collaboration), Phys. Rev. C **68**, 032201 (2003).
[3] K. Joo *et al.* (CLAS Collaboration), Phys. Rev. C **70**, 042201 (2004).
[4] H. Egiyan *et al.* (CLAS Collaboration), Phys. Rev. C **73**, 025204 (2006).
[5] M. Ungaro *et al.* (CLAS Collaboration), Phys. Rev. Lett. **97**, 112003 (2006).
[6] L. C. Smith *et al.* (CLAS Collaboration), in *Proceedings of the Workshop "Shape of Hadrons,"* edited by C. N. Papanicolas and A. M. Bernstein (American Institute of Physics, Boston, 2006), p. 222.
[7] K. Park *et al.* (CLAS Collaboration), Phys. Rev. C **77**, 015208 (2008).
[8] A. Biselli *et al.* (CLAS Collaboration), Phys. Rev. C **78**, 045204 (2008).
[9] M. Ripani *et al.* (CLAS Collaboration), Phys. Rev. Lett. **91**, 022002 (2003).
[10] G. V. Fedotov *et al.* (CLAS Collaboration), Phys. Rev. C **79**, 015204 (2009).
[11] G. V. Fedotov *et al.*, Bull. Russian Acad. Sci. **71**, 328 (2007).
[12] H. Denizli *et al.* (CLAS Collaboration), Phys. Rev. C **76**, 015204 (2007).
[13] R. Thompson *et al.* (CLAS Collaboration), Phys. Rev. Lett. **86**, 1702 (2001).
[14] D. Carman *et al.* (CLAS Collaboration), Phys. Rev. C **79**, 065205 (2009).
[15] D. Carman *et al.* (CLAS Collaboration), Phys. Rev. Lett. **90**, 131804 (2003).
[16] P. Abrozewicz *et al.* (CLAS Collaboration), Phys. Rev. C **75**, 045203 (2007).
[17] V. Burkert and T. S.-H. Lee, in *Electromagnetic Interactions and Hadronic Structure*, edited by F. Close (Cambridge University Press, Cambridge, UK, 2007), p. 77.
[18] V. D. Burkert, in *Proceedings of the 11th Workshop on the Physics of Excited Nucleons, NSTAR2007*, edited by H.-W. Hammer, V. Kleber, U. Thoma, and H. Schmieden (Springer, Berlin, 2008), p. 7.
[19] V. D. Burkert, Prog. Part. Nucl. Phys. **55**, 108 (2005).
[20] G. Penner and U. Mosel, Phys. Rev. C **65**, 055202 (2002).
[21] V. Burkert and T. S.-H. Lee, Int. J. Mod. Phys. E **13**, 1035 (2004).
[22] C. Roberts *et al.*, Eur. Phys J. Special Topics **140**, 53 (2007).
[23] L. Chang *et al.*, arXiv:0906.4304 [nucl-th].
[24] D. Richards, in *Proceedings of the 11th Workshop on the Physics of Excited Nucleons, NSTAR2007*, edited by H.-W. Hammer, V. Kleber, U. Thoma, and H. Schmieden (Springer, Berlin, 2008), p. 40.
[25] H. W. Lin *et al.*, Phys. Rev. D **79**, 034502 (2009).
[26] V. M. Braun *et al.*, Phys. Rev. Lett. **103**, 072001 (2009).
[27] S. J. Brodsky, Light-front QCD, hep-ph/0412101.
[28] D. Merten *et al.*, Eur. Phys. J. A **14**, 477 (2002).
[29] I. G. Aznauryan *et al.*, Theory Support for the Excited Baryon Program at the J lab 12 GeV Upgrade, Jefferson Lab Preprint JLAB-PHY-09-993, arXiv:0907.1901 [nucl-th], [nucl-ex], [hep-lat].
[30] D. Drechsel, S. S. Kamalov, and L. Tiator, Eur. Phys. J. A **34**, 69 (2007).
[31] D. Drechsel, T. Walcher, Rev. Mod. Phys. **80**, 731 (2008).
[32] R. Arndt *et al.*, Eur. Phys. J. A **35**, 311 (2008).
[33] I. G. Aznauryan *et al.* (CLAS Collaboration), Phys. Rev. C **78**, 045209 (2008).
[34] V. D. Burkert, AIP Conf. Proc. **1056**, 348 (2008).
[35] I. G. Aznauryan, V. D. Burkert, H. Egiyan, K. Joo, R. Minehart, and L. C. Smith, Phys. Rev. C **71**, 015201 (2005).
[36] I. G. Aznauryan *et al.*, Phys. Rev. C **67**, 015209 (2003).
[37] K. Wacker *et al.*, Nucl. Phys. **B144**, 269 (1978).
[38] http://www.jlab.org/Hall-B/. CLAS Physics DB.
[39] D. Luke and P. Soding, *Springer Tracts in Modern Physics: Multiple Pion Photoproduction in the s Channel Resonance Region* (Springer, Berlin, 1971), Vol. 59.
[40] J. A. Gomez Tejedor and E. Oset, Nucl. Phys. **A600**, 413 (1996).
[41] L. Y. Murphy and J.-M. Laget, DAPNIA-SPHN-96-10.
[42] M. Hirata, N. Katagiri, and T. Takaki, Phys. Rev. C **67**, 034601 (2003).
[43] A. Fix and H. Arenhovel, Eur. Phys. J. A **25**, 115 (2005).
[44] A. Kiswandhi *et al.*, J. Phys. Conf. Ser. **69**, 012018 (2007).
[45] J. C. Nacher *et al.*, Nucl. Phys. **A695**, 295 (2001).
[46] Y. Assafiri *et al.*, Phys. Rev. Lett. **90**, 222001 (2003).
[47] M. Ripani *et al.*, Nucl. Phys. **A672**, 220 (2000).
[48] V. Mokeev *et al.*, Phys. At. Nucl. **64**, 1292 (2001).
[49] V. Mokeev *et al.*, Phys. At. Nucl. **66**, 1282 (2003).
[50] V. D. Burkert *et al.*, Phys. At. Nucl. **70**, 427 (2007).
[51] I. G. Aznauryan, V. D. Burkert, G. V. Fedotov, B. S. Ishkhanov, and V. I. Mokeev, Phys. Rev. C **72**, 045201 (2005).
[52] V. I. Mokeev *et al.*, in *Proceedings of the Workshop on the Physics of Excited Nucleon, NSTAR2005, Tallahassee, USA, 2005*, edited by S. Capstick, V. Crede, and P. Eugenio (World Scientific, Singapore, 2006), p. 47.
[53] V. I. Mokeev and V. D. Burkert, J. Phys. Conf. Ser **69**, 012019 (2007).
[54] V. I. Mokeev *et al.*, in *Proceedings of the 11th Workshop on the Physics of Excited Nucleons. NSTAR2007*, edited by H.-W. Hammer, V. Kleber, U. Thoma, and H. Schmieden (Springer, Berlin, 2008), p. 76.
[55] V. I. Mokeev *et al.*, arXiv:0906.4081 [hep-ex].
[56] G. V. Fedotov *et al.*, Phys. At. Nucl. **71**, 1309 (2008).
[57] A. Matsuyama, T. Sato, and T.-S. H. Lee, Phys. Rep. **439**, 193 (2007).
[58] T.-S. H. Lee and L. C. Smith, J. Phys. G **34**, S83 (2007).
[59] T.-S. H. Lee, J. Phys. Conf. Ser. **69**, 012013 (2007).
[60] B. Julia-Diaz, T. S. H. Lee, A. Matsuyama, T. Sato, and L. C. Smith, Phys. Rev. C **77**, 045205 (2008).
[61] B. Julia-Diaz *et al.*, Phys. Rev. C **80**, 025207 (2009).
[62] E. Byckling and K. Kajantie, *Particle Kinematics* (John Wiley & Sons, New York, 1972).
[63] E. Amaldi, S. Fubini, and G. Furlan, *Springer Tracts in Modern Physics: Pion Electroproduction*, edited by G. Hohler (Springer-Verlag, Berlin, 1979), Vol. 83.
[64] C. Amsler *et al.*, Phys. Lett. **B667**, 1 (2008).
[65] T. P. Vrana, S. A. Dytman, and T.-S. H. Lee, Phys. Rep. **328**, 181 (2000).
[66] V. D. Burkert, R. DeVita, M. Battaglieri, M. Ripani, and V. Mokeev, Phys. Rev. C **67**, 035204 (2003).
[67] K. Gottfried and J. D. Jackson, Nuovo Cimento **34**, 736 (1964).
[68] T. Sato and T.-S. H. Lee, Phys. Rev. C **63**, 055201 (2001).

[69] F. Cano and P. González, Phys. Lett. **B431**, 270 (1998).
[70] A. Bartl, W. Majerotto, and D. Schildknecht, Nuovo Cimento A **12**, 703 (1972).
[71] R. Machleidt, in Advances in Nuclear Physics, **19** (1979).
[72] C. J. Bebek *et al.*, Phys. Rev. D **17**, 1693 (1978).
[73] M. Vanderhaeghen, M. Guidal, and J. M. Laget, Phys. Rev. C **57**, 1454 (1998).
[74] R. Longacre and I. Dolbeu, Nucl. Phys. **B122**, 493 (1977).